



This is a repository copy of *Studies of Isolated and Non-isolated Photospheric Bright Points in an Active Region Observed by the New Vacuum Solar Telescope*.

White Rose Research Online URL for this paper:
<http://eprints.whiterose.ac.uk/129657/>

Version: Published Version

Article:

Liu, Y., Xiang, Y., Erdelyi, R. et al. (6 more authors) (2018) Studies of Isolated and Non-isolated Photospheric Bright Points in an Active Region Observed by the New Vacuum Solar Telescope. *Astrophysical Journal*, 856 (1). ISSN 0004-637X

<https://doi.org/10.3847/1538-4357/aab150>

Reuse

Items deposited in White Rose Research Online are protected by copyright, with all rights reserved unless indicated otherwise. They may be downloaded and/or printed for private study, or other acts as permitted by national copyright laws. The publisher or other rights holders may allow further reproduction and re-use of the full text version. This is indicated by the licence information on the White Rose Research Online record for the item.

Takedown

If you consider content in White Rose Research Online to be in breach of UK law, please notify us by emailing eprints@whiterose.ac.uk including the URL of the record and the reason for the withdrawal request.



eprints@whiterose.ac.uk
<https://eprints.whiterose.ac.uk/>



Studies of Isolated and Non-isolated Photospheric Bright Points in an Active Region Observed by the New Vacuum Solar Telescope

Yanxiao Liu^{1,2,3} , Yongyuan Xiang^{1,3} , Robertus Erdélyi^{4,5} , Zhong Liu^{1,3}, Dong Li^{6,7} , Zongjun Ning^{6,7} , Yi Bi^{1,2,3} ,
Ning Wu⁸, and Jun Lin^{1,3} 

¹ Yunnan Observatories, Chinese Academy of Sciences, P.O. Box 110, Kunming, Yunnan 650216, People's Republic of China; jlin@ynao.ac.cn

² University of Chinese Academy of Sciences, Beijing 100039, People's Republic of China

³ Center for Astronomical Mega-Science, Chinese Academy of Sciences, Beijing, 100012, People's Republic of China

⁴ Solar Physics and Space Plasma Research Centre (SP2RC), School of Mathematics and Statistics, The University of Sheffield, Hicks Building, Hounsfield Road, Sheffield S3 7RH, UK

⁵ Department of Astronomy, Eötvös University, Pázmány P. sétány 1/A Budapest P.O. Box 32, H-1117, Hungary

⁶ Purple Mountain Observatory, Chinese Academy of Sciences, Nanjing, Jiangsu 210008, People's Republic of China

⁷ Key Laboratory of Dark Matter and Space Science, Chinese Academy of Science, Nanjing, Jiangsu 210008, People's Republic of China

⁸ School of Tourism and Geography, Yunnan Normal University, Kunming, Yunnan 650500, People's Republic of China

Received 2017 May 7; revised 2018 February 17; accepted 2018 February 19; published 2018 March 21

Abstract

Properties of photospheric bright points (BPs) near an active region have been studied in TiO λ 7058 Å images observed by the New Vacuum Solar Telescope of the Yunnan Observatories. We developed a novel recognition method that was used to identify and track 2010 BPs. The observed evolving BPs are classified into isolated (individual) and non-isolated (where multiple BPs are observed to display splitting and merging behaviors) sets. About 35.1% of BPs are non-isolated. For both isolated and non-isolated BPs, the brightness varies from 0.8 to 1.3 times the average background intensity and follows a Gaussian distribution. The lifetimes of BPs follow a log-normal distribution, with characteristic lifetimes of (267 ± 140) s and (421 ± 255) s, respectively. Their size also follows log-normal distribution, with an average size of about $(2.15 \pm 0.74) \times 10^4$ km² and $(3.00 \pm 1.31) \times 10^4$ km² for area, and (163 ± 27) km and (191 ± 40) km for diameter, respectively. Our results indicate that regions with strong background magnetic field have higher BP number density and higher BP area coverage than regions with weak background field. Apparently, the brightness/size of BPs does not depend on the background field. Lifetimes in regions with strong background magnetic field are shorter than those in regions with weak background field, on average.

Key words: instrumentation: high angular resolution – methods: observational – Sun: photosphere

1. Introduction

The solar photosphere is covered by numerous grain-like structures, known as granules, due to energy transportation from the inside of the Sun to its surface being dominated by convection. Many small and bright features are observed to appear in the inter-granule lanes, and studies of these features can be tracked back to the 1970s (e.g., see Dunn & Zirker 1973 and Mehlretter 1974 for a brief review). Nowadays, these bright features are known as photospheric bright points, or bright points (BPs) for short.

BPs often have a brightness ratio of 0.8 ~ 1.8 relative to the nearby surroundings of the quiet Sun (e.g., see Sánchez Almeida et al. 2004). Usually, BPs of high intensity contrast are observed in the G-band (4300 Å) continuum, a spectral band dominated by the CH molecule (see Grevesse & Sauval 1973). The enhanced brightness contrast of BPs in the G-band is due to a reduction of the CH abundance by dissociation in the deep photospheric layers of the flux tubes. With weakening of CH-lines, more photons in the continuum are allowed to escape from the deep photosphere through the flux tubes, and brightening in the G-band CH-lines consequently is observed easily (see Steiner et al. 2001 and Schüssler et al. 2003 for more discussions). Steiner et al. (2001) further suggested that other molecular bands or atomic lines may exhibit a similar behavior. Depletion of molecules in the magnetic flux concentrations was found to take place in the range of wavelengths from 3000 to 7000 Å in numerical experiments carried out by Rutten et al. (2001).

In addition to the G-band, the spectral line TiO λ 7058 Å is also used to observe BPs (Cao et al. 2010; Liu et al. 2014). TiO λ 7058 Å possesses a wavelength longer than that of the G-band. According to the standard theory of turbulence measurements regarding the seeing of the atmosphere, the longer the working wavelength λ , the better the seeing of the surrounding environment (see also Tatarskii 1961 and Roddier 1981). More quantitatively, the Fried (1966) parameter, r_0 , of the seeing depends on λ in the way of $r_0 \propto \lambda^{6/5}$ (refer to Tokovinin & Kornilov 2007), which yields that the seeing for the observation in TiO λ 7058 Å is better than that in the G-band for ground-based telescopes. Therefore, we also choose to observe BPs in TiO.

Dunn & Zirker (1973) and Mehlretter (1974) were the first to systematically investigate various manifestations and properties of the bright features at the center and the far wing of the H α and CaII K spectral lines, respectively. They looked into locations, sizes, lifetimes, magnetic field, etc., of these features, and pointed out that these bright features usually appeared as individual points and could have forms of “filigree” and “crinkles.” They noticed that these features generally possessed a size of 200 ~ 300 km in diameter, lifetimes of around 2 ~ 3 minutes for the small points and up to 27 minutes for the large-scale ones, and a strong magnetic field of 100 ~ 1000 G near the crinkle (as opposed to 2000 G in the network postulated by Stenflo 1973 and up to 3000 G in active regions estimated by Harvey & Martin 1973).

The strong magnetic fields of BPs are usually believed to result from the convective motion in the photosphere that pushes magnetic elements into inter-granule lanes and inter-sections, leading to the formation of clusters and the concentration of magnetic field in the photosphere. However, the convective effect alone could not cause a concentration compact enough to contain a sufficiently strong magnetic field, meaning the strong magnetic field also results from the convective instability in the flux tube (Nagata et al. 2008; Fischer et al. 2016). Cooling of the plasma inside the tube, due to the thermal irradiance, yields a downward flow because of gravity, in turn causing the pressure inside the flux tube to decrease. The difference in total pressure between the outside and inside invokes the instability of the tube, which leads to further concentration of the magnetic field inside the flux tube, and the tube eventually is stabilized as the magnetic field inside becomes strong enough. This process is known as the collapse of the magnetic flux tube as a result of convection, which was confirmed in two-dimensional numerical experiments by Grossmann-Doerth et al. (1998). An inverse course may happen as well, when the plasma inside the tube moves upward, associating with the growing instability of the tube, and concludes with the dispersion of the magnetic field and the disappearance of the tube (see the discussions of Roberts & Webb 1979; Spruit 1979; Spruit & Zweibel 1979; Unno & Ando 1979).

Spruit & Zweibel (1979) argued that the convective collapse could only take place in a region where the magnetic field is weak enough. They noticed that a flux tube in an adiabatic state may become convectively unstable as the magnetic field inside becomes weaker than a critical strength, say 1270 G. Observations by Hinode suggested a magnetic field of about 1.3 kG in flux tubes (see also Utz et al. 2013). A recent numerical simulation performed by Criscuoli & Uitenbroek (2014) showed that the magnetic field in these thin tubes observed in the G-band is typically a few kG. Therefore, most of these flux tubes are stable.

Spruit (1979) further investigated the behavior of various parameters for flux tubes at their collapsed state. He found that, in addition to the stronger magnetic field inside the tube, the temperature in the tube is slightly lower than that of the environment in the deep sub-photospheric layer, but the former temperature exceeds the latter in the layer very close to the surface. The consequence of such a distribution of these parameters in the tube is twofold: first of all, the approximate blackbody property in this region suggests that a high temperature results in strong emission; second, cold plasma with low density inside the flux tube falls down and lowers the surface of the optical depth unity to deeper layers at higher temperatures. This further leads to the increased heating from the granular walls and produces the brighter appearance of the flux tube near the surface (see also Keller et al. 2004; Vögler et al. 2004; Steiner 2005). Numerical experiments of Hewitt et al. (2014) captured these observational results well.

Therefore, a BP is the interaction of a magnetic flux tube with the photosphere, and can thus be thought of as a tracer of the footprint of magnetic flux tubes in the photosphere (Berger et al. 1998; De Pontieu 2002; Schüssler et al. 2003; Beck et al. 2007; Yang et al. 2016). BPs, therefore, play a key role in helping to investigate various behaviors of the magnetic elements in the photosphere, and further our understanding the physics of these behaviors. Thus, the importance of

studying the BP is threefold: first of all, BPs are tightly related to the magnetic field in the same atmosphere (Mehlretter 1974; Ishikawa et al. 2007), so their kinematic behaviors and manifestations should also reveal important information about the energy conversion and transportation from the photosphere to the upper atmosphere, and help identify the energy source responsible for chromosphere and coronal heating, as well as the storage of energy in the corona that could drive large-scale eruptions. Second, as the smallest structure that present telescopes can resolve, BPs allow us to investigate the physical properties of magnetic elements in the layers below the photosphere. Third, how much the BP brightness could contribute to the total irradiance of the Sun is still an open question and worth studying in detail. Fully investigating the motions of BPs is essential for understanding the reaction of the above-lying atmospheric layers; not only for wave phenomena propagating within BPs, but also magnetic field braiding and/or reconnection.

Furthermore, the style of mass motion in the photosphere indicates that BPs move in a somewhat random fashion (Abramenko et al. 2011; Jafarzadeh et al. 2014; Yang et al. 2015). Observations indicate that BPs are pushed passively inside inter-granular lanes, which oscillate successively under the buffeting of granules, exciting magnetohydrodynamic (MHD) waves that propagate upward through flux tubes and transport energy into the chromosphere and the corona (e.g., see also Fedun et al. 2011; van Ballegoijen et al. 2011; Vigeesh et al. 2012). According to this scenario, van Ballegoijen et al. (2011) developed a three-dimensional model, which showed that Alfvén wave turbulence could be created by the internal random motion of flux tube footpoints. Jess et al. (2009) showed strong observational evidence that the Alfvén wave was very likely to be invoked by the motion of the flux tube footpoints, which could transport enough energy into the chromosphere and the low corona to heat these regions of the solar atmosphere (see also Mumford & Erdélyi 2015; Mumford et al. 2015, as confirming support).

To analyze the behavior of BPs, and understand their role in energy storage in connection to solar eruption and the small-scale reconnection responsible for the heating of the chromosphere and corona, we first need to identify and track them. Several useful and efficient algorithms have been developed for identifying BPs in recent years. A multiple-scale pattern recognition algorithm (Bovelet & Wiehr 2001, 2007) was used to identify both bright and faint BPs, allowing BPs to be extracted through intensity contrast and size thresholds (Bovelet & Wiehr 2003, 2007; Wiehr & Bovelet 2009). Utz et al. (2009) used high-intensity contrasts, large-intensity gradients, and small sizes to identify BPs through segmentation, clean-up, and recognition. In the work of Crockett et al. (2009), a feature would be identified as a BP if both the longest span of a bright feature is less than seven pixels and the gradient calculated in eight directions exceeds a given threshold; the size of the identified BP was then obtained by applying a region growth algorithm (see also Crockett et al. 2010). Feng et al. (2012) selected the candidate seed regions by convolving the original image with a Laplacian filter, and then determined the boundary and size of BPs after the regions around these seeds were expanded via a morphological dilation operation.

We note here that these algorithms identify BPs in different ways, and each of them possesses its own strengths and

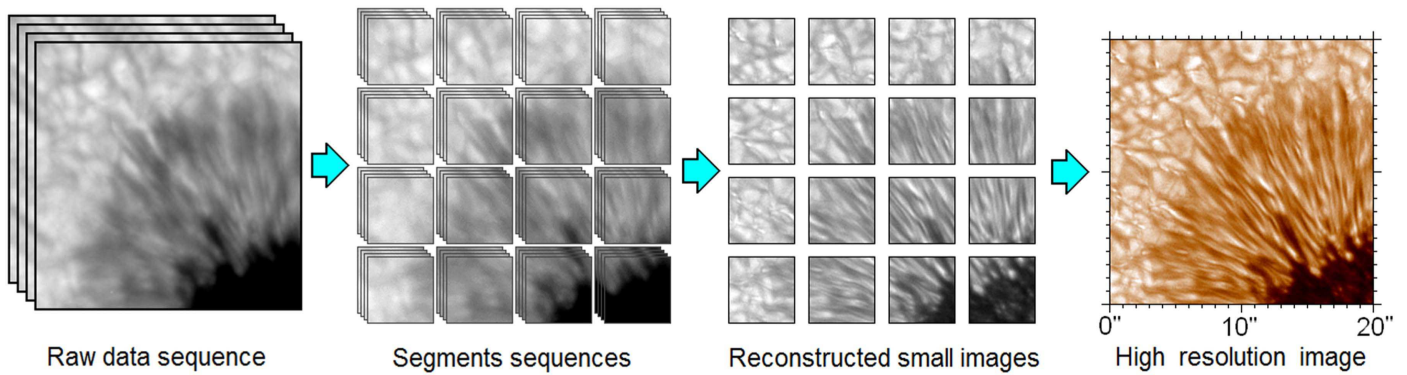


Figure 1. Schematic description of the image reconstruction process. Left: sliced-up image from the raw data; middle-left: raw data image; middle-right: segments of an image for which the reconstruction has been completed; right: resultant image of the whole area after reconstruction.

weaknesses. However, a common weakness they share is that they mainly focus on isolated BPs (hereafter iBPs), i.e., a BP that does not experience either merging or splitting during its lifetime. Obviously, splitting and merging make the BP evolution complicated and difficult to track. This is probably the reason why previous works avoided studying non-isolated BPs (hereafter niBPs). As we shall notice later, many BPs undergo splitting and merging at least once in their lifetimes, which implies that many BPs are niBPs, and our knowledge obtained from previous works on BPs has room for improvement. This means that we have to identify both the iBPs and niBPs simultaneously when looking into various features and properties of BPs. Therefore, in addition to studying the properties of BPs, a large amount of our effort involved in this work is invested in developing a new algorithm that can identify and track both iBPs and niBPs, which will allow us to investigate BPs in a more comprehensive fashion than before.

In the present work, we use data obtained near an active region by the New Vacuum Solar Telescope (NVST) of the Yunnan Observatories. In Section 2, we briefly describe the raw data and the reconstruction methodology of high-resolution images from the raw data, and we introduce the algorithm we have developed to recognize and track BPs. We present our results in Section 3, discuss these findings in Section 4, and finally summarize this work in Section 5.

2. Observations and Data Processing

The data studied here were obtained by the NVST (Liu et al. 2014), located at the Fuxian Lake in Chengjiang County, Yunnan Province, China. The telescope possesses a clear aperture of 985 mm. The good seeing of the site allows us to perform investigations of fine structures in the photosphere and the chromosphere, even though the adaptive optical (AO) technique had not been applied when the observation was performed (see Liu et al. 2014 and references therein for detailed discussions on this issue). What we observed for this work is an area near active region AR 11748 with very good seeing ($r_0 \approx 10.628$ cm). The observation was performed in a field of view (FOV) of 69×62 arcsec² in TiO λ 7058 Å, and the data cover the time interval from 06:13:50 to 08:59:00 UT on 2013 May 21, without interruption, at a cadence of 25 s and pixel size of $0''.039$. Some of the data, obtained with very stable seeing and good image quality in the time interval from 06:13:50 to 06:59:00 UT, are studied in this work.

2.1. Raw Data Processing

We cannot immediately use the raw data, obtained by the NVST, to study BPs because the images have been randomly and rapidly degraded by turbulence in the atmosphere of the Earth, which is a major problem of ground-based telescopes, especially for a telescope with large aperture like NVST. The raw data of NVST were reconstructed using the high-resolution reconstruction algorithm with the speckle-masking method to obtain high-resolution images (Weigelt 1977; Weigelt & Wornitzer 1983).

We start the high-resolution reconstruction by selecting at least 100 images taken successively with short exposures, e.g., less than 10 ms, in the present work. We then cut each of these images into many, e.g., 16 sequence segments of 5×5 arcsec² (see the first two panels in Figure 1), to match the isoplanatic angle of the Earth atmosphere (for more details, see Xiang et al. 2016). At the third step, we conduct image reconstruction for the sequences of 100 5×5 arcsec² images to obtain 16 5×5 arcsec² small images of high resolution. Finally, merging these 16 segments together gives a large image of the whole area of interest with high resolution. All the detectors equipped at the NVST are sensitive enough to ensure the cadence of the raw data be shorter than 10 s. A high-quality image needs at least 100 exposure images to reconstruct, which requires cadence of at least 100 exposures. The real cadence of reconstructed images is actually constrained by the cadence of the raw data sequence, so the cadence of the reconstructed data used in this work is 25 s.

2.2. Alignment

With the reconstruction completed, we need to spatially align the NVST and *SDO*/HMI data. The alignment performed here includes two pieces of work, namely alignment among the NVST data themselves and alignment between the NVST data and the *SDO*/HMI data.

Let us first perform the alignment among the NVST data. As shown in the left panel of Figure 2, a window containing sunspots is chosen first, and then the cross-correlation is performed between two neighboring frames. The offsets in the x - and y -directions with highest barycenter correlation coefficients are obtained, and the images are aligned to each other according to the offsets. The precision of the alignment achieves the level of sub-pixel accuracy (see also Feng et al. 2012; Yang et al. 2015).

We are now able to look into fine structures in the lower solar atmosphere. The left panel in Figure 2 displays a

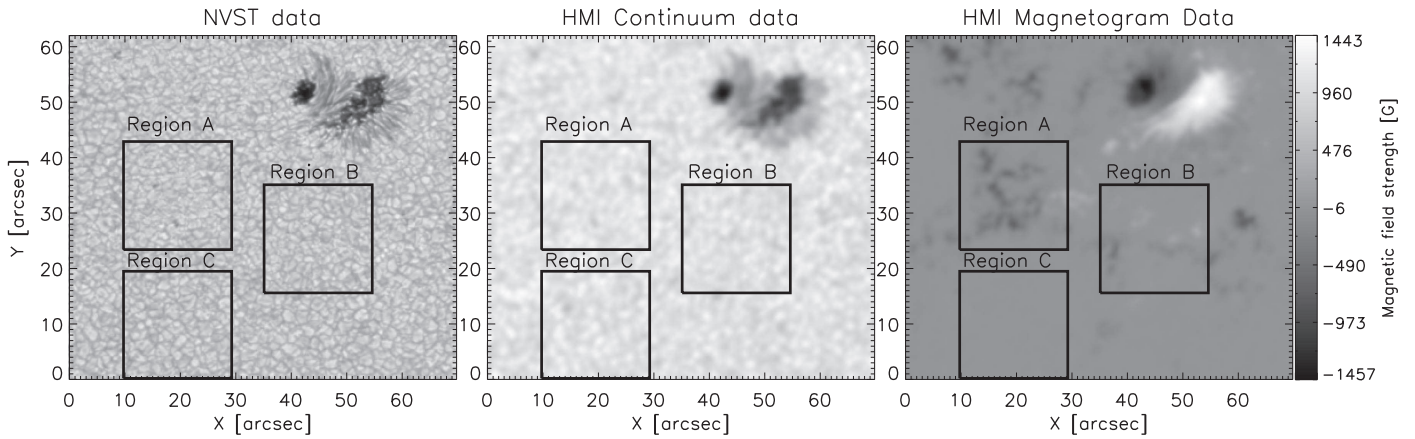


Figure 2. The left panel is a reconstructed NVST image of the region studied. The middle and right panels are the aligned HMI continuum data and HMI magnetogram data, respectively. The three regions (A, B, C) are marked separately in each of the three panels.

reconstructed image of the region we study in this work. In this data set, a pair of sunspots and three groups of pores can be recognized. We notice that BPs around sunspots are distributed in an apparently non-uniform fashion. As shown in the left panel in Figure 2, three regions surrounded by black squares are selected for detailed studies because BPs in these regions display markedly different behaviors. The most BPs are measured in Region A, fewer are detected in Region B, and Region C contains the least BPs (see also Figure 3). We also notice that Region A includes some pores, but no big BPs; no pore appears in Region B, but some big BPs can be recognized in this region; and BPs in Region C were small and faint.

Meanwhile, we also look at the magnetic fields in these three regions taken by *SDO/HMI* (Schou et al. 2011). First, we pre-processed the HMI data using SSW in order to improve the quality of the images. Second, we enhanced the pixel resolution of the HMI data from $0''.6 \text{ pixel}^{-1}$ to $0''.039 \text{ pixel}^{-1}$ via cubic convolution interpolation, with the cubic parameter equal to -0.5 so that the processed HMI data could have a pixel scale comparable to that of the NVST data. Third, we took the sunspots at the upper-right corner of both the NVST image and the HMI continuum image (see that in the middle panel in Figure 2) as a reference to perform the alignment via cross-correlation. This is the alignment performed for the NVST data to the HMI continuum data (see also Feng et al. 2017 for more details).

In order to estimate the error of the alignment, we cut one NVST image into many 100×100 pixel boxes and align them separately to the HMI image via the same approach. The offset values in the x - and y -directions are obtained for each box. If the NVST data is aligned well with the HMI data, these boxes should have the same offsets—in principle. In reality, on the other hand, error always exists because of the noise of individual images, as well as the fact that the data analyzed here were from different atmosphere layers, and were obtained by different instruments. The average offsets of these boxes in x - and y -directions are obtained, and they are used to finally align the HMI and NVST images. The alignment errors, here, are determined by the largest difference between the offsets of these boxes and the average offsets. We found the offset error for the alignment in this work to be 1.032 pixels in the x -direction and 0.955 pixels in the y -direction, respectively.

After the above operation, we now know that the images in the left and middle panels of Figure 2 cover the same area of interest. We further cut a section of the image from the HMI magnetogram that coincides with the same area of the HMI continuum image as shown in the right panel in Figure 2, and the alignment of the NVST image to the HMI magnetogram is automatically completed because both of them are aligned to the HMI continuum image.

In addition to the left panel in Figure 2, we also marked Regions A, B, and C correspondingly in the other two panels in Figure 2. Now we are ready to look into BPs in the three regions mentioned above, and investigate various properties of BPs and the nearby areas. The panels in the upper row of Figure 3 display the NVST images of these three regions, respectively; those in the lower row display the corresponding HMI magnetograms. As expected, Region A includes the strongest magnetic field, ranging from $-659 \pm 18 \text{ G}$ to $292 \pm 18 \text{ G}$, with an average strength of $-103 \pm 18 \text{ G}$. The magnetic field in Region B varies from $-413 \pm 18 \text{ G}$ to $248 \pm 18 \text{ G}$, with an average of $-4 \pm 18 \text{ G}$, and in Region C it varies from $-37 \pm 18 \text{ G}$ to $40 \pm 18 \text{ G}$ with an average of $-1 \pm 18 \text{ G}$, respectively. In the work described in the following section, we identify all the BPs in the data, followed by studying them in detail.

2.3. Identifying and Tracking BPs

BPs near active regions appear as laminal structures, and are called laminal BPs, chains (Sánchez Almeida et al. 2004), or filigrees (Berger et al. 1995; Pietarila et al. 2009). Laminal BPs are those BP features that are elongated along the inter-granule lanes. The values of their areas disperse in a large range, and their brightness also displays oscillatory behavior. Therefore, laminal BPs might be removed if we were to use the conventional methods and algorithms for identifying the isolated BPs when the traditional size and brightness thresholds would be applied. To avoid removing laminal and/or faint BPs because of false diagnosis, we developed a new approach to dealing with, identifying, and tracking all the BPs, including laminal and faint ones. Our new algorithm for identifying and tracking all the BPs consists of seven steps, and they are described as follows.

Step one, convolve the original images (the left panel in Figure 4) with a Laplace filter. The Laplace filter is an isotropic second-order differential operator. The isotropy means that the

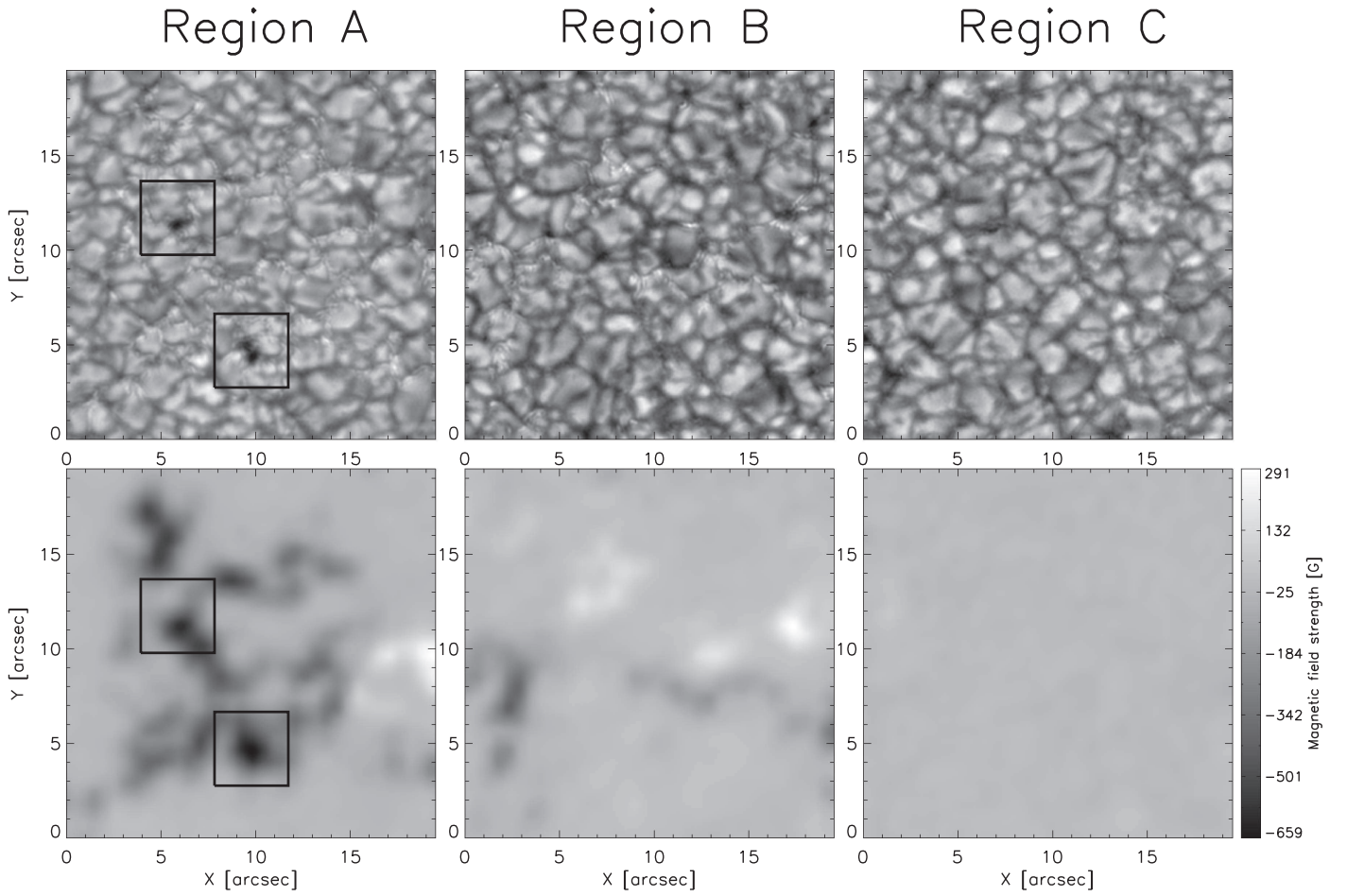


Figure 3. Upper row: images of the three selected regions A, B, and C of Figure 2 from NVST data. The areas in region A containing pores are emphasized with black squares, and the same regions in HMI magnetogram are marked correspondingly. Middle: region B, including BP ribbons. Right: “quiet” region C, located far from the sunspot. Lower row: the corresponding magnetograms of the same regions taken by *SDO/HMI*.

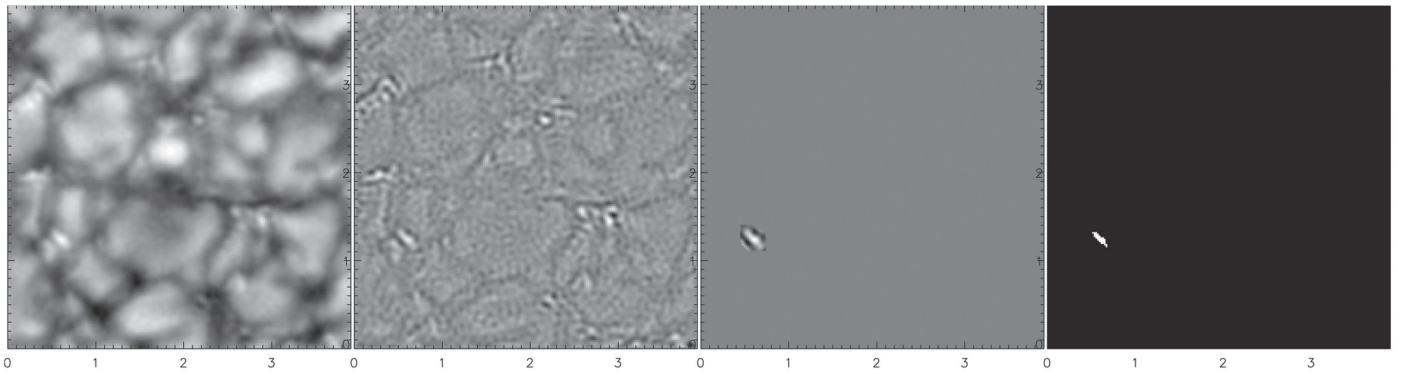


Figure 4. From left to right, the first panel is a small region of the original image. The second image shows the Laplace convolution. The BPs are clearly visible and are extracted in this image. The third panel is a bright point in a window opened by dilation operation from the Laplace image, while the last panel is the extracted bright point from the small window showed in the third panel.

effect of first performing the convolution and then rotating the resultant image is the same as that of performing the rotation first and then convolving the resultant image. The Laplace filter highlights the region including intensity discontinuities and deemphasizes the region of small intensity gradient (for more details, see Gonzalez & Woods 2008).

In a digital image, the Laplacian of function $f(x, y)$ with two variables is defined as:

$$\nabla^2 f(x, y) = \partial^2 f(x, y) / \partial x^2 + \partial^2 f(x, y) / \partial y^2, \quad (1)$$

and its discrete form is

$$\nabla^2 f(x, y) = f(x + 1, y) + f(x - 1, y) - 2f(x, y) \quad (2)$$

in the x -direction, and

$$\nabla^2 f(x, y) = f(x, y + 1) + f(x, y - 1) - 2f(x, y) \quad (3)$$

in the y -direction. In applications, the discrete Laplacian of function $f(x, y)$ usually takes the form:

$$\nabla^2 f(x, y) = [f(x + 1, y) + f(x - 1, y) + f(x, y + 1) + f(x, y - 1)] - 4f(x, y). \quad (4)$$

In a digital image, a pixel has left, right, up, and down neighboring pixels, which are called the four neighbor pixels. Therefore, Equation (4) is the so-called four-neighbor Laplacian of an image referring to these neighboring pixels in x - and y -directions, respectively. Similarly, we can also construct a so-called eight-neighbor Laplacian, such as

$$\nabla^2 f(x, y) = [f(x + 1, y) + f(x + 1, y + 1) + f(x + 1, y - 1) + f(x - 1, y + 1) + f(x - 1, y - 1) + f(x - 1, y) + f(x, y + 1) + f(x, y - 1)] - 8f(x, y), \quad (5)$$

which further includes four neighbors in the diagonal directions. The Laplace filter masks corresponding to Equations (4) and (5) are

$$L = \begin{Bmatrix} 0 & -1 & 0 \\ -1 & 4 & -1 \\ 0 & -1 & 0 \end{Bmatrix}, \quad (6)$$

and

$$L = \begin{Bmatrix} -1 & -1 & -1 \\ -1 & 8 & -1 \\ -1 & -1 & -1 \end{Bmatrix}, \quad (7)$$

respectively. We note here that the sign of the Laplacian in Equations (6) and (7) is opposite to that of the traditional Laplacian related to Equations (4) and (5) in order to achieve “positive/bright” values for BPs. Performing the convolution of the original image with the Laplacian filter in Equation (6) or Equation (7) gives three types of results: positive, negative, and zero. In the case that four (or eight) times the value of the brightness of a given pixel in the original image is greater than the sum of the values of four (or eight) neighboring pixels, the convolution gives a positive result, meaning that this pixel is brighter than its surroundings; in the case of the opposite situation, where we have a negative result, the pixel selected is fainter than its surroundings; the result is zero if the selected pixel is as bright as its surroundings.

Generally, the brightness gradient of granules is smaller than that of BPs, the convolution performed above helps to emphasize the BP and de-emphasize the granules. Basically, both Laplacians in Equations (6) and (7) can perform the job well, but the Laplacian in Equation (7) is unnecessarily sensitive to some unimportant details and may bring extra noise, so we use Laplacian (6) in this work.

In step two, we extract the bright structures with a proper threshold. Here, the threshold value is determined according to the result of convolving of the image with the Laplace kernel. This threshold should allow us to extract the most BP seeds that mix with the least granules. The threshold for an image is determined such a way that, if the highest convolution value of the image is I_{\max} , then the threshold for that image is $0.1 \times I_{\max}$. The pixels with convolution values higher than this threshold are kept as seeds. Most of them are candidate BPs, and the remains could be very bright granules.

Step three, remove noise. Those seeds that are located in bright granules are called noise here because they are not the target that we are interested in and need to be removed. The noise possesses the obvious features of having a short “lifetime” and occupying a small area of just a few pixels. The “lifetime,” here, is determined as the time duration of a candidate seed consecutively appearing. In this work, seeds of “lifetime” less than 75 s or size less than five pixels are removed as noises. Although this process removes some true BP candidate seeds as well, they can be identified at a later step when the BP is tracked.

Step four, extract faint BP seeds in the region of interest. Some BPs display changing brightness, so a faint BP at a given time might be a bright one earlier or later, and they might be missed at step two because their convolution values could be lower than the threshold. In a time-sequence of images processed by Laplacian convolution, we pinpoint an identified BP seed region in a selected image and open a “window” via the dilation operation at the same position in the previous or next image. Then, with a new threshold, we check whether a BP seed exists in the window (see the middle-left panel in Figure 4). If no BP seed is detected, the operation stops here. Otherwise, we continue to extract the faint BPs.

Here, the new threshold used to check whether a BP seed exists is determined in the following way. First, let us calculate the convolution of the image with the Laplacian given in Equation (6). We then calculate convolutions of the image with the x - and y -components of the Laplacian associated with Equations (2) and (3), but with opposite signs, respectively. Once all the images are processed this way, the new threshold is determined at the levels of all the three-values of the convolution results obtained at this step. In this work, the new threshold is taken as 150. If any of the three convolution values of a pixel in the region is lower than 150, this pixel is discarded. If all three of the convolution values exceed 150, this pixel is marked as detected. If a blob consists of more than 10 marked pixels, this blob is marked as a new candidate BP seed; if the marked blob includes less than 10 pixels, we consider this region candidate BP seed absent and stop further operation on it. We complete step four by iterating all the above operations to all the identified BP seed regions.

Step five, find BP edges to obtain the real size of a selected BP. BPs that stay in dark inter-granule lanes have a very large intensity gradient at the edge, corresponding to the zero crossing in the Laplacian of the image (namely, the local intensity maximum of the first-order derivative corresponds to the zero crossing of the second-order derivative). However, some BPs that stay close to one another or to granules may have neither a large intensity gradient at the edge nor a zero crossing in the Laplacian of the image. Furthermore, we also noticed that some bright pieces of granules may also mix with these BPs. Therefore, extra attention needs to be paid in this case. We point out that the brightness normally still changes fastest across the edge of BP, with the first derivative reaching its maximum and the zero crossing of the second derivative. By means of this property, we are capable of locating the edge of BPs inside inter-granule lanes.

First of all, we open a “window” of suitable size that includes a BP seed region and the pixels around the region (see the middle-right panel in Figure 4). In the “window,” we evaluate the first and second derivatives of the brightness distribution in both the x - and y -directions inside the window,

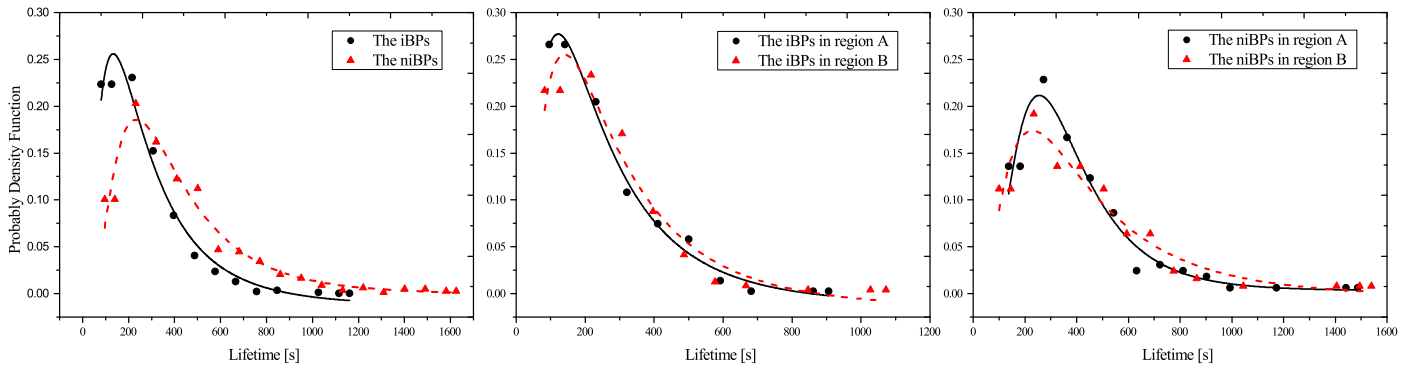


Figure 5. Lifetime distributions of BPs. Black dots and red triangles are for observational results and the solid/dashed curves are log-normal fittings to the observational results. Left: lifetime distributions of all the iBPs/niBPs (black dots/red triangles). Middle: lifetime distributions of the iBPs in Regions A (black dots) and B (red triangles), respectively. Right: those of the niBPs in Regions A (black dots) and B (red triangles), respectively.

then locate the pixels as the edge pixels at which, in either x - or y -direction, the first derivatives reach maximum and the second derivatives cross zero. These pixels, thus, constitute the edge of BP. So far, the task of recognizing BPs using our new algorithm has been completed. Next is to track the identified BPs in their motions and evolutions.

Step six is to track the identified BPs. This is a very important step because the deduced lifetime and velocity of BPs are dependent not only on the identification, but also on the tracking. Some BPs move at different velocities in different directions; others stay close to one another to form clusters, merge, or split into smaller BPs. Such complicated evolutionary behavior brings much difficulty to the existing algorithm for tracking a selected BP. Therefore, we need to advance the existing algorithm to allow us to be able to track the identified BPs. With this algorithm, we first check the identified BPs in the above processed time-sequence image. If BPs at two successive frames overlap, we consider these two BPs to be the same one but at different times. We then move on to the next consecutive image.

Step seven, classify BPs into iBPs and niBPs. The method to distinguish the iBPs from the niBPs is straightforward because the former does not split or merge, while the latter BP does. In our algorithm used here, they are identified/distinguished in the following way: if the position where a BP was identified at a given time was occupied by two or more BPs in the next image of the sequence, then we consider that splitting of a BP has occurred or is occurring; if the position where two or more BPs were identified earlier was then occupied by a single BP later, on the other hand, we consider that merging of BPs has taken place or is ongoing.

In both these latter cases, the BPs are classified as niBPs. If no such process occurred to a BP during its lifetime, such a BP is considered as an iBP. However, generally speaking, it is not easy to distinguish splitting of BPs from merging by using our current algorithm alone, because some BPs may split and merge several times during their lifetimes, which results in a fairly complex evolution process. Once this part of the work has been completed, we are ready to study the kinematic features and properties of identified BPs, including both the iBPs and niBPs.

3. Results

Applying the algorithm outlined above to BPs in the regions outside the sunspot, as shown in Figure 2, we identified and tracked 2010 evolving BPs, among which 1306 (i.e.,

64.9%) are iBPs, and the remaining 704 are niBPs. In the whole image with an FOV of 69×62 arcsec², only a small region was covered by the sunspots. The region without sunspots covers an area of 2151.9 Mm², and we identify and track BPs in the spotless region. For each image, we are able to calculate the total number of identified individual BPs per unit area, i.e., the number density of BPs at a given time, from which we obtain an average density over the time interval that our data covers of 0.25 BPs Mm⁻².

Let us now focus on BPs appearing in the three regions indicated by black rectangles A, B, and C, as shown in Figures 2 and 3. There are 404 evolving BPs in Region A with 65.5% being iBPs and 34.5% being niBPs, 297 evolving BPs in Region B with 62.9% iBPs and 37.1% niBPs, and 19 evolving BPs in Region C with 18 iBPs, respectively. Furthermore, we also calculate the occupied area coverage of BPs in the entire region without sunspots, including regions A, B, and C. Here, the area coverage is determined by the total area of all identified BPs divided by the area of this region. We find that the area coverage is 0.57% for the entire region, 1.1% for Region A, 0.82% for Region B, and 0.04% for Region C, respectively.

3.1. Lifetime of BPs

Usually, splitting or merging is considered as the end or the beginning of the lifetime of an evolving BP. We argue, in this work, that the time when a BP experiences splitting or merging should not be considered as the disintegration of an old BP or the birth of new one. Instead, they are in fact a special stage of the BP evolution. As these BPs are reliable tracers of the flux tube footpoints, the study of splitting and merging behavior of magnetic flux tubes helps us better understand how the photospheric magnetic flux tubes evolve. Therefore, the lifetime of an evolving BP, T , is defined in this work as the period from the time when it appears for the first time to the time when it completely disappears, no matter how many splits or merges this evolving BP has experienced.

We studied the lifetime distributions of both iBPs and niBPs within our sample of 2010 BPs. In Figure 5, the left panel shows all the iBPs/niBPs (black dots/red triangles). The middle one is for the iBPs in Regions A (black dots) and B (red triangles), and the right panel shows the distributions of niBPs in Regions A (black dots) and B (red triangles). There are very few evolving BPs identified in Region C (only 19 in total), which may not be a high enough sample rate for statistics.

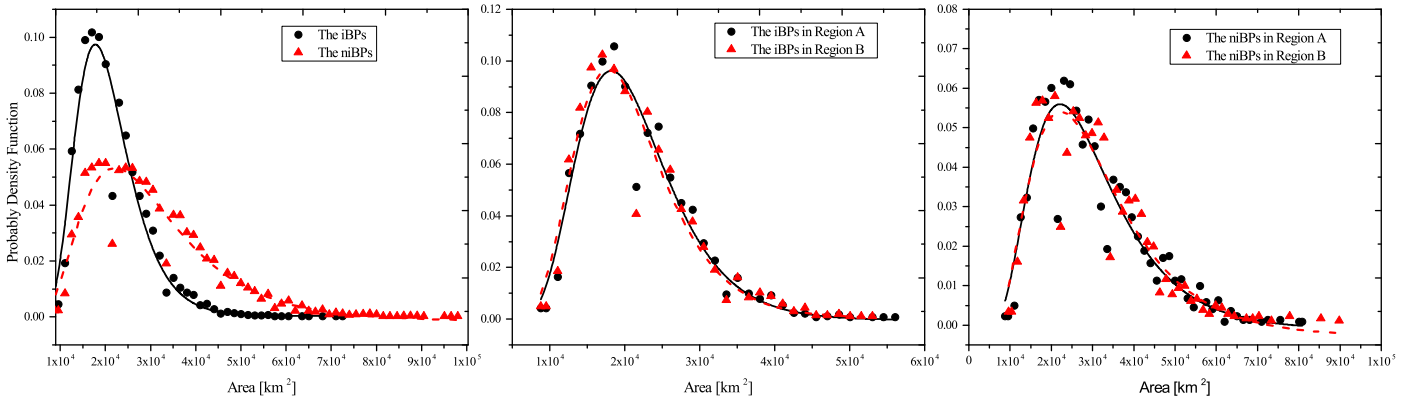


Figure 6. Same as Figure 5, but for the area distribution of BPs.

Table 1
Lifetimes [in s] of Evolving BPs Studied in This Work

	Average	10% Longest
iBPs	267 ± 140 (all ^a)	459
	257 ± 131 (A ^b), 263 ± 135 (B ^c), 289 ± 116 (C ^d)	
NiBPs	421 ± 255 (all ^e)	769
	401 ± 212 (A), 412 ± 244 (B), 486 (C)	
All the evolving BPs	320 ± 203	567

Notes.

^a For all iBPs.

^b For evolving BPs in Region A.

^c For evolving BPs in Region B.

^d For evolving BPs in Region C.

^e For all niBPs.

Therefore, we do not conduct detailed investigations for BPs in Region C.

The left panel in Figure 5 indicates that iBPs with black dots and niBPs with red triangles are fitted by log-normal distributions (black solid/red dashed curves), respectively. Table 1 shows that the average lifetime of iBPs is 267 ± 140 s. About 10% of iBPs last longer than 459 s. For the niBPs, the average lifetime is about 421 ± 255 s, and about 10% of niBPs live longer than 769 s.

The middle panel in Figure 5 displays the lifetime of iBPs in Regions A and B with black dots and red triangles, respectively. The fitting lines show that iBPs in Regions A and B both follow log-normal distributions and they have almost the same pattern of distribution, which is similar to those of the niBPs in the right panel. Comparing the niBPs with iBPs, the lifetime distribution of niBPs has a longer tail than iBPs, indicating that the niBPs contain more long-lived BPs (see the middle and right panels).

Table 1 shows that the average lifetimes of the iBPs in Regions A, B, and C are about 257 ± 131 s, 263 ± 135 s, and 289 ± 116 s, respectively. The average lifetimes of niBPs in Regions A, B, and C are about 401 ± 212 s, 412 ± 244 s, and 486 s, respectively. For all the evolving BPs, including iBPs and niBPs, the average lifetime is about 320 ± 203 s. The lifetimes of about 10% of all these evolving BPs are longer than 567 s (see also Table 1). Table 1 also reveals that the

average lifetime of the iBPs in Region A is shorter than that of those in Region B, which is also true for the niBPs.

3.2. Area of BPs

We are now ready to study the area variation of evolving BPs, including both the iBPs and niBPs. The areas are calculated in a simple way. The iBP consists of a series of snapshot BPs along time sequence. For each snapshot of a BP, we just need to determine the area occupied by all the pixels in the snapshot of this BP. To estimate the areas of niBPs, we follow the same method. The difference is, however, that the niBPs experience merging and splitting during their lifetimes. For this reason, we just determine the area that all the related individual BPs occupy in a given frame.

After obtaining areas, we are now able to further perform statistical analyses. Two methods have been considered. The first one is to look into the mean area of each evolving BP over its lifetime and to perform the statistical studies of the mean areas of all the evolving BPs. The second one is to focus on the area of each evolving BP at every single time, and to investigate the statistical behaviors of all these areas. Obviously, the second approach provides more samples than the first one, and we stay with the second one in the present work.

Figure 6 displays the area distributions of the iBPs and niBPs in the entire FOV, and in Regions A and B, respectively. The black dots (red triangles) in the left panel show the area distribution of all the iBPs (niBPs). The black solid and red dashed curves are the corresponding log-normal fittings to the observation results. The middle panel of Figure 6 shows that the area distributions of the iBP follow a log-normal distribution in both Regions A and B, with almost the same distribution pattern. For the niBP in the right panel, the area distributions also follow log-normal distributions, but differences in the detailed distribution patterns for Regions A and B could be recognized. Because there were not enough BP samples in Region C, we do not make separate plots for them.

We now turn to analyze the average area of BPs. The average area of all the BPs at all snapshots for iBPs is $(2.15 \pm 0.74) \times 10^4 \text{ km}^2$, and for niBPs it is about $(3.00 \pm 1.31) \times 10^4 \text{ km}^2$. About 10% of the snapshot BPs have areas larger than $7.67 \times 10^4 \text{ km}^2$ for the iBP, and larger than $12.3 \times 10^4 \text{ km}^2$ for niBPs. The average BP areas of the iBP in Regions A, B, and C are $(2.18 \pm 0.73) \times 10^4 \text{ km}^2$, $(2.16 \pm 0.75) \times 10^4 \text{ km}^2$, and $(2.10 \pm 0.61) \times 10^4 \text{ km}^2$, respectively, and those of the niBP are $(2.95 \pm 1.23) \times 10^4 \text{ km}^2$,

Table 2
Areas (in 10^4 km^2) of BPs

	Average	10% largest
iBPs	$2.15 \pm 0.74(\text{all}^a)$	7.67
	2.18 ± 0.73 (A), 2.16 ± 0.75 (B), 2.10 ± 0.61 (C)	
niBPs	3.00 ± 1.31 (all)	12.3
	2.95 ± 1.23 (A), 2.97 ± 1.28 (B), 2.42 ± 0.81 (C)	

Note.

^a The same notes apply here as for Table 1.

$(2.97 \pm 1.28) \times 10^4 \text{ km}^2$, and $(2.42 \pm 0.81) \times 10^4 \text{ km}^2$, respectively (see also Table 2).

We also calculate the equivalent diameters of BPs following the same method as for the area. Figure 7 displays the diameter distributions of the iBP/niBP with dots/triangles, respectively. It is clear that both iBPs and niBPs follow log-normal distributions as well (see the solid and dashed curves in Figure 7); the average diameters and the standard deviations are found to be $163 \pm 27 \text{ km}$ for iBPs, and $191 \pm 40 \text{ km}$ for niBPs.

Furthermore, we study the distribution of the diameters of iBPs at their first appearance in time, at the time they vanish, and at the moment of their maximum sizes. The left panel in Figure 8 shows these three distributions for the iBPs. We notice that the diameters at the first moment of appearance and at the time of vanishing have similar distribution patterns. These distributions are fitted with the same log-normal function shown as the solid curve. The dashed histogram is the size distribution of iBPs at the maximum sizes in their lifetimes, fitted by a log-normal and marked by a dashed curve. The right panel shows the ratio distributions of the size at the time of disappearance to that at their first appearance (dashed histogram), and the size at their maximum to that at the first appearance (solid histogram). We noticed that the distribution of the size ratio at the time of vanishing to that at their first appearance in time could be fitted well by a Gaussian function, which ranges from 0.5 to 1.9. On the other hand, the distribution of the size ratio at maximum to that at their first appearance is fitted by the log-normal function, which ranges from 1 to 2.3.

3.3. Intensity Contrast

The BP intensity (or brightness) contrast, C_0 , is defined in this work by

$$C_0 = (I_a - I_q)/I_q, \quad (8)$$

where I_a is the average intensity of a snapshot BP, and I_q is the average background intensity of a very quiet region in the same frame. The quiet region selected is far from sunspots, pores, and magnetic knots; it contains only granules and a few BPs. For an evolving BP, the intensity contrast of the snapshot BPs in each frame is calculated.

Figure 9 plots the distributions of C_0 for iBPs and niBPs in the entire FOV, and Regions A and B, respectively. In the left panel of Figure 9, the black dots (red triangles) are the intensity contrast distribution of iBPs (niBPs). Both distributions are fitted by a Gaussian function with black solid and red dashed curves, respectively. The middle panel shows the distributions

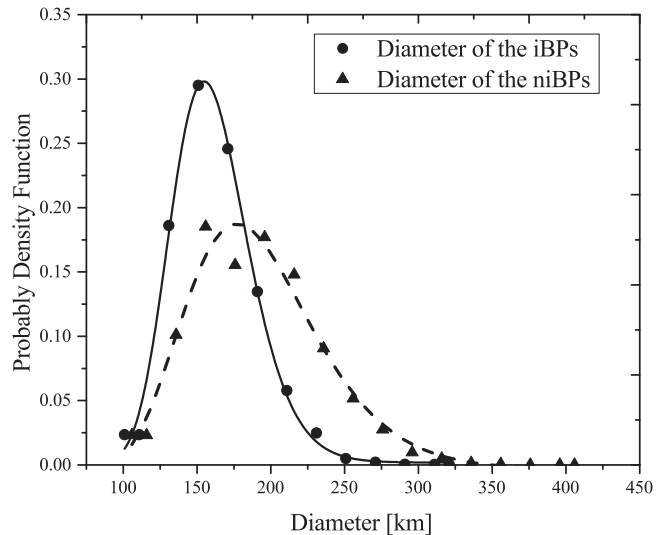


Figure 7. The diameter of BPs. The black dots are the diameter of iBPs fitted by log-normal function (solid curve). The triangles are the diameter of niBPs fitted by a log-normal function (dashed curve).

of C_0 of iBPs in Regions A (black dots) and B (red triangles). The results indicate that the intensity contrast distribution for iBPs in Region A follows a pattern similar to that of iBPs in Region B. The same statement can be made about niBPs in Regions A and B (see the right panel in Figure 9).

We note, here, that some values of C_0 are negative. This implies that the corresponding BPs should not be recognizable. However, this paradox can be solved as follows: according to Equation (8), it is clear that negative values occur when $I_a < I_q$, which indicates that the average brightness of a corresponding BP is lower than the average background intensity. This reveals that such BPs are faint. However, they are still brighter than the inter-granule lanes in the surroundings and possess sharp edge gradients. Therefore, a BP with a negative value of C_0 is still recognizable.

Table 3 lists the mean and the standard deviation displayed in Figure 9. The intensity contrasts of both the niBPs and iBPs follow well a Gaussian distribution with mean values and standard deviations of 0.104 ± 0.045 and 0.084 ± 0.047 , respectively. Obviously, the distributions for iBPs in Regions A and B have almost the same pattern, with mean values of 0.002 ± 0.031 (Region A) and 0.002 ± 0.028 (Region B), respectively, which is similar to that for niBPs, with mean values of 0.004 ± 0.028 in both Regions A and B. About 10% of iBPs have an intensity contrast larger than 0.144, and 10% of niBPs have one larger than 0.160.

3.4. Rotation of BPs

From the data we collected in the present work, we have identified two types of rotating motions of BPs: a spin of the feature around itself, as well as vortex flows/whirl flows on slightly larger scales within which the BPs can participate. The former has not been reported yet, to the best of our knowledge, but the latter is more widely studied (Balmaceda et al. 2010; Steiner et al. 2010; Shelyag et al. 2011). Details of these two kinds of rotating motion of BPs will be investigated in this section.

We start with the first case, i.e., the spin, or changes in orientation of elongated BPs, as shown in Figure 10. We identified a small representative BP that is highlighted by the

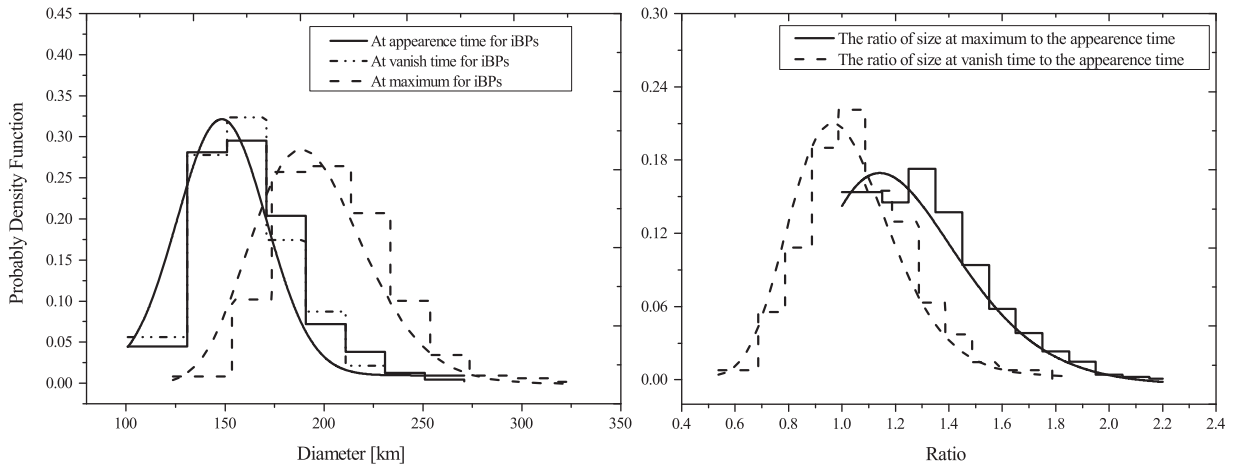


Figure 8. Left panel: the diameter distributions of BPs at their first appearance time (solid histogram), at the time they vanished (dash-dot-dotted histogram), and at maximum (dashed histogram), respectively. Right panel: the ratios of size at the time of vanishing to that at the time of first appearance (dashed histogram), and the maximum sizes to that at first appearance time (solid histogram). The solid and dashed curves are corresponding log-normal fittings in both left and right panels.

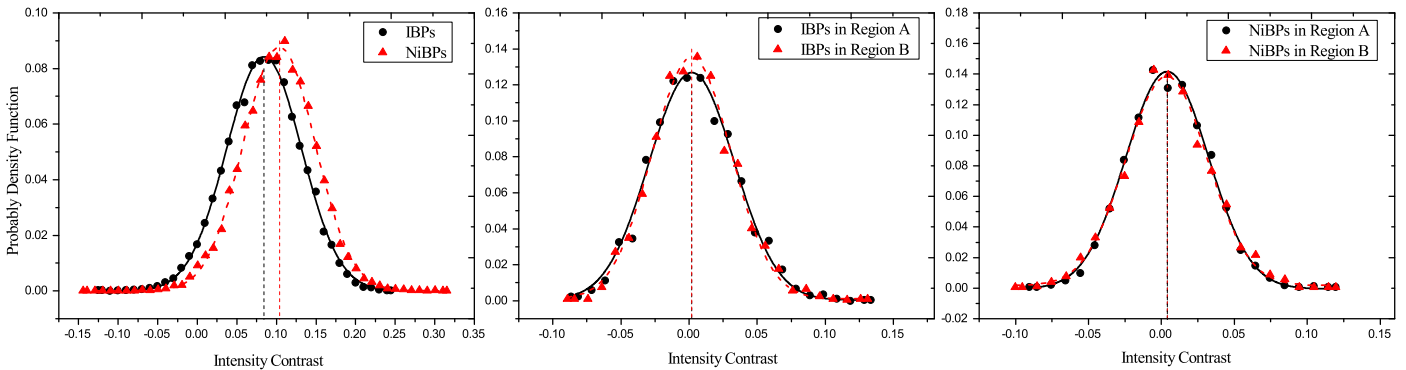


Figure 9. Intensity contrast, C_0 , distributions of all the iBPs and niBPs. Discrete points are the result of C_0 deduced from Equation (8) on the basis of observations, and the black solid/red dashed curves are Gaussian profiles fitted to the discrete points. Left: plots for all the iBPs/niBPs (black dots/red triangles). Middle: plots for the iBPs in Regions A (black dots) and B (red triangles). Right: plots for the niBPs in Regions A (black dots) and B (red triangles).

Table 3

Fitting Parameters of Intensity Contrast for the iBPs and niBPs

	Mean (μ)	10% Largest Intensity Contrast
iBPs	$0.084 \pm 0.047(\text{all}^a)$	0.144
	0.002 ± 0.031 (A), 0.002 ± 0.028 (B)	
niBPs	$0.104 \pm 0.045(\text{all})$	0.160
	0.004 ± 0.028 (A), 0.004 ± 0.028 (B)	

Note.

^a The same notes apply here as for Table 1.

red circle in panel (a). The angle between the orientation of this BP and the horizontal direction of the figure was $123^\circ.7$ at 06:27:46 UT. This BP stayed in a dark inter-granule lane separating three small granules. We noticed that there was a faint, small-sized granule, to the left of the BP, that was gradually expanding its width and length (see panels (a)–(c)). During this time, the angle changed to $113^\circ.4$ (comparing panels (a) and (c)) clockwise. The BP then became smaller and turned its shape from laminal into round (see panel (d)). Meanwhile, the granule to the left of the BP expanded and

became closer to the BP. As a result, the inter-granule lane was narrower than before and ultimately could barely contain the BP (see panel (e)).

Next, the BP turned its shape into laminal again, in accord with the width of the inter-granule lane, while simultaneously changing its orientation. We noticed that the orientation now became $76^\circ.8$. The BP was pushed continuously in the narrow inter-granule lane by the two nearby granules, and the BP brightness was consequently enhanced. In this process, the BP changed its shape and orientation back and forth successively, as a result of the granule convection.

Aside from successively changing their orientations due to the convection of granules, vortex motions are another important source that contributes to BP rotations. As shown in Figure 11, a laminal BP surrounded by the large red circle (Figure 11(a)) first split into two smaller ones, and these two small BPs moved together clockwise around a granule. At the beginning, the leading BP moved faster than the following one (Figures 11(b) through (e)); the motion of the following BP then accelerated and it caught up with the leading one, whereupon they again merged into single large BP (Figures 11(f) through (h)). Meanwhile, this large BP and a smaller BP nearby moved together toward a granule to their right. With their approach, the granule vanished, and the two BPs eventually occupied the location of the granule. At the same time, the part of BPs in the small red circle quickly

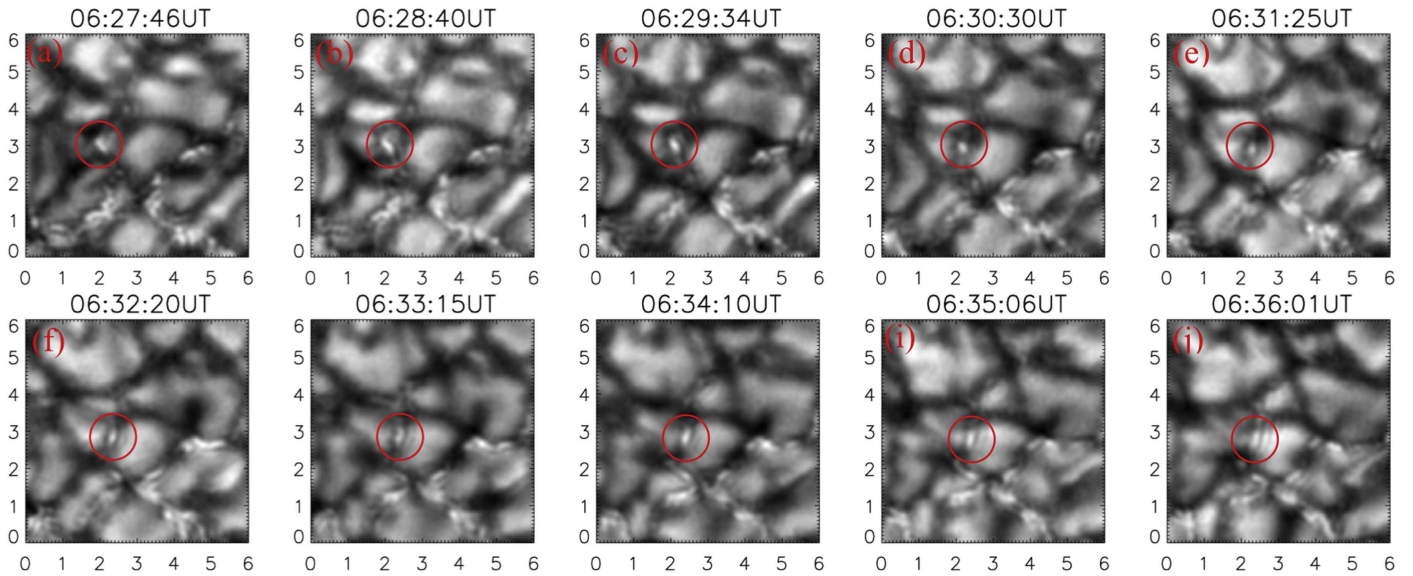


Figure 10. The first case of a rotating BP. A BP is inside the red circle. The time is marked at the top of each snapshot. Initially, the BP was in a direction pointing toward the upper left corner of the image before it turned its direction toward the top right corner, as finally demonstrated in panel (f).

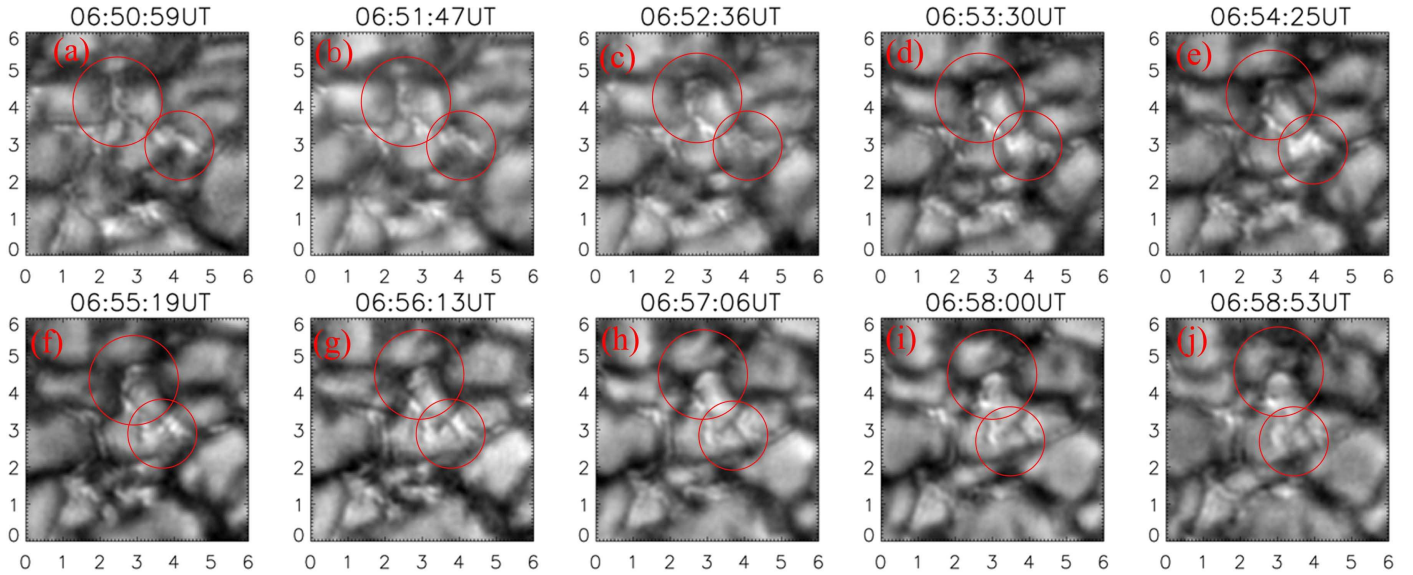


Figure 11. The vortex motion of BPs. Example of five BPs driven clockwise by vortex motions. Three BPs move clockwise around the same granule before breaking it up. The fourth BP moves into the granule and appears to change that granule's shape.

moved clockwise toward the granule to their left side and pushed it into a special shape.

In the first case studied in this sub-section, we found that a BP was pushed into a laminal structure between two granules, and then changed shape to be small and circular a few minutes later. The BP was then compressed into a laminal BP in another direction. In the second case, we analyzed four BPs rotating clockwise. Three of them were around the same granule, and ultimately broke it. The fourth BP moved clockwise and pushed itself into the granule in its left side. The shape of the granule was changed because of the rotating motion of the BP.

3.5. Merging and Splitting of NiBPs

Let us now investigate three cases of niBP: merging, splitting, and merging while also splitting back and forth. We are convinced that merging and splitting should be a popular

kinematic feature of BPs. One reason why there are few reports on this topic is that tracking of these BPs was usually stopped before a BP started merging and/or splitting, and the merging and splitting was regarded as the death of an old BP or the birth of new one.

Figure 12 shows the first case, i.e., BPs merging. There were five faint, small BPs at the beginning, as shown in panel (a), and they remain in the intersection of four granules. They continued to concentrate in a compact region for 25 s (see panel (b)), and eventually merged into a single laminal BP within another 24 s (see panel (c)). In this process, it is hard to tell whether the granule convection or gas pressure contribute to the merging because the granules around did not manifest apparent changes in size and brightness in the first 25 s (comparing panels (a) and (b)). In the evolution from panels (b) to (c), the granule below the BPs could be seen to expand toward the BPs, and started squeezing the BPs in the direction

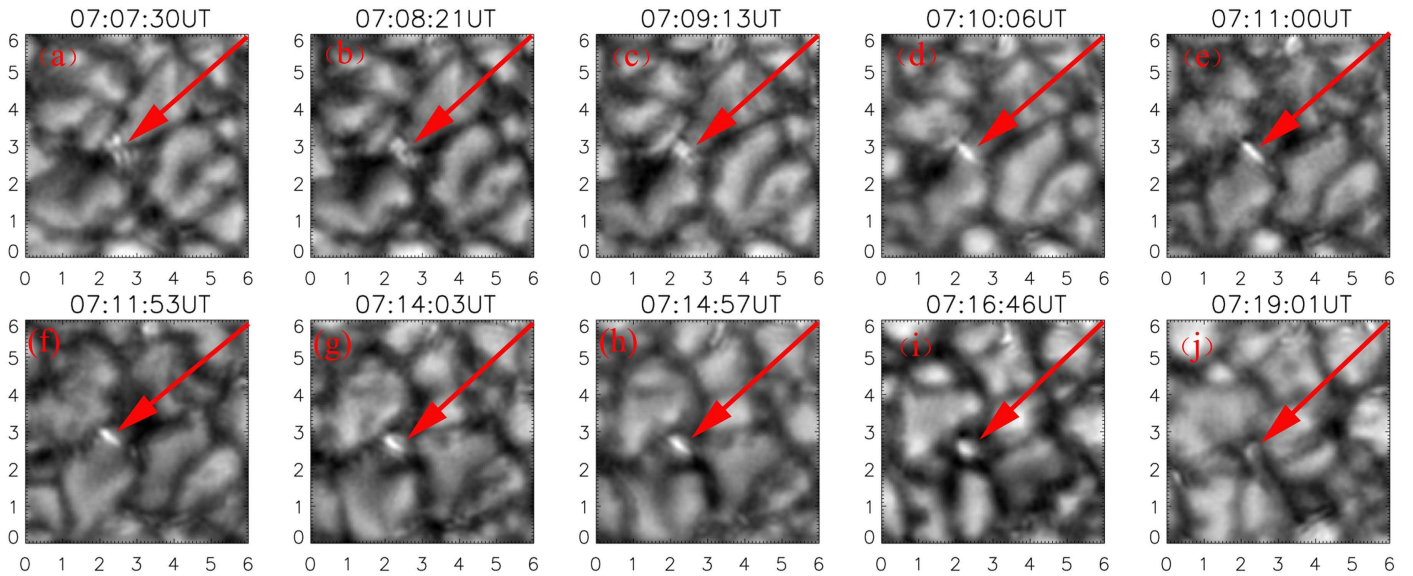


Figure 12. Sample of merging BPs. There are five faint, small BPs staying at the intersection of four granules. Four BPs merge into one large BP within 51 s; they enhance its brightness due to the compression as two granules move toward one another.

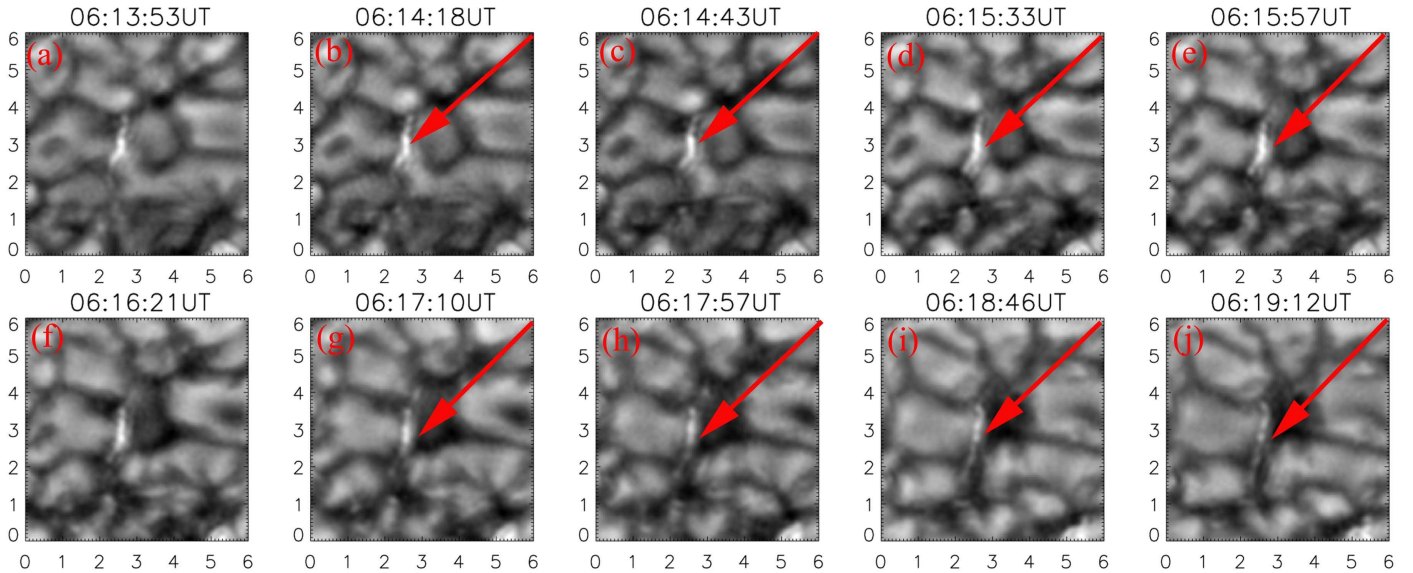


Figure 13. Sample of splitting BPs. There is a laminal BP located in a narrow inter-granule lane (see panel (a)). The laminal BP becomes fainter and fainter, then splits into several small BPs. These small BPs disappear one by one.

normal to that of BP merging. About 103 s later, the inter-granule lanes around the BPs apparently became narrower than before (comparing panels (c) and (d)) because two granules at two sides of the BPs started moving toward one another, squeezing the BP further, and the process of BP merging was completed. Meanwhile, the brightness of the resultant BP increased (comparing panels (c) and (d)), and the BP brightness stayed at a maximum for about 400 s before it became faint again (comparing panels (d) through (h)). Finally, the resultant BP gradually disappeared in the following 244 s (see panels (h) through (j)).

During the entire merging process, we see clearly how the compression of granules contributes to the brightness of the merged BP. When granules moved away and the inter-granule lane became wider, the BP changed its shape into a circular one and turned faint until its complete disappearance. However, we are not entirely sure in this case whether the granule

compression was fully responsible for the merging behavior of BPs. As we have mentioned previously (see also Figure 11), the alternate scenario may occur: i.e., that two small BPs chase each other, where the leading BP moves slower than the following one, and the two eventually collide and merge into a new, single BP. However, more effort needs to be invested in studying this issue further in the future.

Figure 13 displays a simple and straightforward case of BP splitting. The process started with a laminal BP, which has fully filled an inter-granule lane, as marked by the arrow. There were two small, faint BPs farther over the top. Two granules were located at the right side of the BPs, and one granule was observed at the left side (see panels (a)). The small BPs and the laminal one maintained their brightness unchanged over the following 99 s (see panels (b)–(e)). The left granule expanded its size while the laminal BP became fainter and fainter, and eventually split into five small faint BPs. Meanwhile, one of the

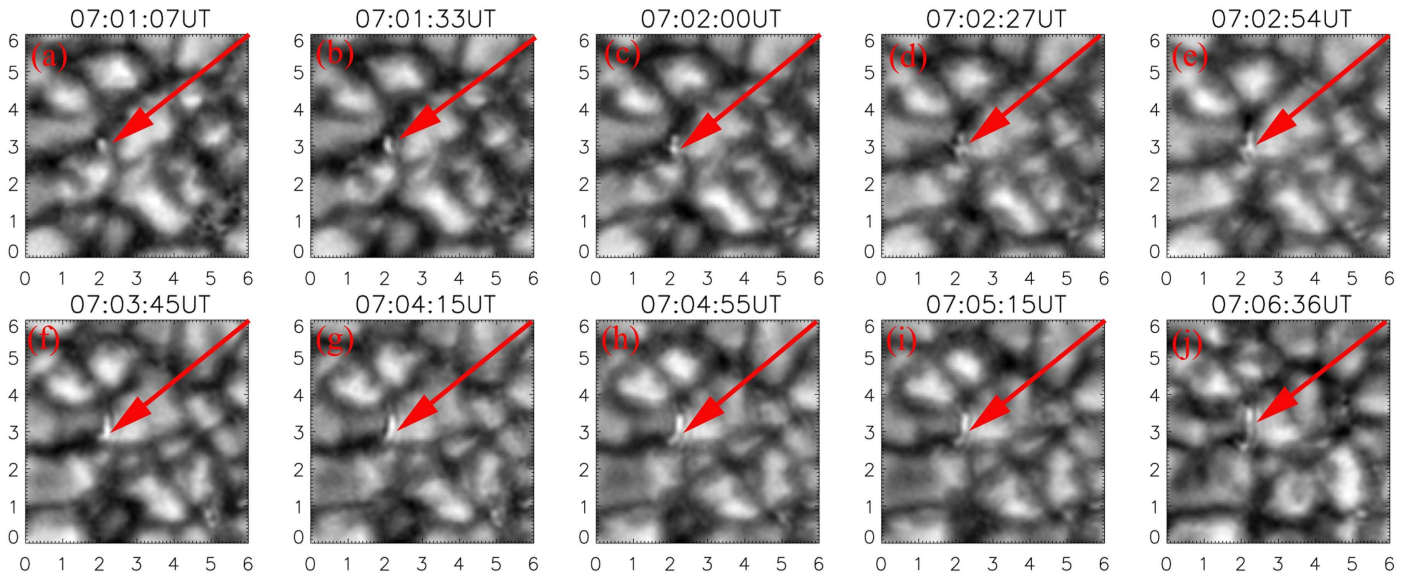


Figure 14. Example of a splitting BP accompanied by merging. A circular BP located in an intersection of three granules is elongated into a laminal shape and splits into two small BPs (see panels (a)–(c)). These two small BPs move together and merge again. The merged BP is compressed into a laminal structure by two granules (see panels (f)–(h)). The merged BP finally splits into two BPs again (see panels (i) and (j)).

two granules at the right side disappeared (see panels (e) and (j)). All of the small BPs then disappeared one by one. In this process, the brightness of the laminal BP was not uniform. The parts of the BPs closer to the two sides of the granule edges were brighter than the other parts at the ends of the laminal BP (see also panel (a)).

Figure 14 displays a more complex case where merging and splitting of BPs took place a couple of times during the lifetime. We note here that this work is mainly focused on describing various kinematic behaviors of BPs, and does not focus on the physics behind merging and splitting of BPs. The physical interpretation of these fairly complicated phenomena/processes in the evolution of BPs is beyond the scope of the current study.

A circular BP was located in the intersection of three granules at the beginning (see panel (a)). It was then elongated into a laminal BP over the following 26 s (panel (b)). After that, the BP split into two small BPs at the time of 53 s. Within these 53 s, the BP experienced two processes: elongating and splitting. The two small BPs then moved closer to the right-side granule, and the inter-granule lanes, where the two small BPs were located, became narrower than before (comparing panels (c)–(e)). In the time interval taken between snapshots of panels (d) to (e), the two BPs came closer and merged fully, as seen in panel (f). The duration of the entire merging process is about 78 s. In this process, the three granules around the two small BPs expanded in size and the inter-granule lane became narrower and narrower. Two granules among these three pushed the resultant BP further into a laminal shape and further enhanced the BP’s brightness. The resultant BP then split again, such that part of the merged BP was torn away (comparing panels (i) and (j)). Eventually, both parts of the BP disappeared.

4. Discussion

In this work, we have developed a new algorithm for identifying and tracking photospheric evolving BPs on the basis of some existing algorithms. This new algorithm has

some advantages over the existing ones. First of all, faint BPs are extracted by our algorithm as long as an evolving BP is detected in three consecutive sequence of images. The evolving BP can then be tracked during its lifetime, no matter whether its brightness changes or not. Second, the snapshot BP edges could be determined nicely even when a snapshot BP is close to bright granules or to the other snapshot BPs. Third, iBPs and niBPs could be classified by using this algorithm.

BPs are reliable tracers of those footpoints of the upper solar atmospheric magnetic configurations that are rooted in the photosphere. The kinematic and dynamic behavior of these footpoints affect geometric structures and evolutionary features of the upper solar atmospheric magnetic fields, as well as the energy transportation from the photosphere to upper solar atmosphere. Thus, identifying and classifying evolving BPs is of significant importance for understanding chromospheric and coronal heating, as well as the energy accumulation in the upper solar atmosphere for solar eruptions.

Applying this algorithm, we identified and tracked a total of 2010 evolving BPs in the entire region we selected. Among them, 35.1% are niBPs that experienced either splitting or merging during their lifetimes, and 65.9% are iBPs that have not experienced either splitting or merging during their lifetimes. In Region A, the identified and tracked BPs include 65.5% iBPs and 34.5% niBPs. In Region B, the iBPs’ and niBPs’ shares are 62.9% and 37.1%, respectively. The shares of the two types of BPs in Regions A and B do not differ from one another, although the background field in these regions are different. Muller (1983) found that about 15% of evolving BPs in their study were subject to fragmentation, but no merging was observed. Muller & Roundier (1992) further reported that about 15%–30% of BPs split, which is lower than the 35.1% obtained here, but they did not observe BP merging.

The number density of snapshot BPs for the entire FOV deduced in this work is about 0.25 Mm^{-2} on average. This result is slightly lower than others found in the literature: 0.32 BP Mm^{-2} (Feng et al. 2012) and 0.38 BP Mm^{-2} (Keys et al. 2011) in the active region, and 0.3 BP Mm^{-2} (Sánchez Almeida et al. 2004) and 0.97 Mm^{-2} (Sánchez Almeida

et al. 2010) in the quiet Sun. We found that the number density of BPs was different in each of the three regions studied here. The BP number densities in Regions A, B, and C are 0.46 Mm^{-2} , 0.38 Mm^{-2} , and 0.02 Mm^{-2} , respectively. We also found the BP area coverage to be about 1.1%, 0.82%, and 0.04% for Regions A, B and C, respectively. Ji et al. (2016) reported area coverage of BPs varying from 0.2% to 1.99% in their work, and Feng et al. (2012) found 1.3% in the active region and 0.7% in the quiet Sun. The distributions of number density and area coverage of BPs suggest that the both the number density and area coverage of BPs vary along with the strength of background magnetic fields (see also Figures 2 and 3, as well as the related content given before). We noticed that distributions of BPs in the quieter region (Region C) are more tenuous than the porous region (Region A) or the ribbon region (Region B).

Lifetimes of both the iBPs and niBPs follow log-normal distributions, analyzed separately in the full FOV and in Regions A and B. The average lifetimes of iBPs and niBPs are $267 \pm 140 \text{ s}$ and $421 \pm 255 \text{ s}$, respectively. The former is consistent with that of $243 \pm 127 \text{ s}$, obtained from 50 evolving BPs in the active region by Möstl et al. (2006). The lifetime of iBPs obtained in this work is longer than $150 \pm 3 \text{ s}$ (Utz et al. 2010), but shorter than 552 s (Nisenson et al. 2006). The iBPs have average lifetimes of $257 \pm 131 \text{ s}$, $263 \pm 135 \text{ s}$, $289 \pm 116 \text{ s}$ in Regions A, B, and C, respectively. This reveals that iBPs in regions with stronger background magnetic field tend to have shorter lifetimes, which is true for the niBPs as well (see details in Table 1). However, this is inconsistent with the results reported in Keys et al. (2011) who found that BPs live longer in the region with stronger background magnetic field. Furthermore, we notice that the niBPs contain more long-lived, evolving BPs than iBPs (also see Figure 5 and Table 1).

Considering the fact that variable seeing might affect measurements of the size and brightness of BP snapshots, and could even affect other results obtained in this work, we performed a set of tests to quantify how the changing seeing would influence the results we obtained. We noticed that the seeing parameter r_0 in the period of the data studied here had a mean value of 10.628 cm, with a standard deviation of 0.220 cm.

According to the variation of r_0 in this period, we divided the data into 21 groups in such a way that images in the same group have the same r_0 values (with deviation not exceeding 0.003 cm). Grouping the data in this way guarantees that the fluctuation of the BP parameters in the same group is not caused by fluctuations of the seeing. Furthermore, classifying the images into different groups helps enhance the signal/noise ratio.

From the data in each group, we were able to obtain a mean value, μ_0 , for the parameter of interest, and we eventually could identify 21 values of μ_0 for this parameter. The random behavior of BPs implies that these 21 values should not differ from one another within the permitted range of error, if the seeing did not change in the period when the observation was performed. In reality, however, the seeing varies with time, so the value of μ_0 changes from group to group. In other words, fluctuations in the obtained μ_0 indicate the change in r_0 , in a certain sense.

Following this idea, we deduce 21 values of μ_0 for the area and relative brightness, respectively, of the identified and tracked BPs. Here, the relative brightness of BPs is defined as

I_a/I_q (cf. Equation (8)). Next, for both the area and the relative brightness, we can further evaluate the average, μ , of the 21 values of μ_0 and the associated standard deviation, σ . We find $\mu \pm \sigma = (1.511 \pm 0.030) \times 10^4 \text{ km}^2$ for the area and 1.084 ± 0.003 for the relative brightness, respectively. These results suggest that deviations in measurements of the area and the relative brightness of BPs as a results of the fluctuation in r_0 are 5.0% and 0.3%, respectively, which indicates a limited impact of the changing seeing on the area and the relative brightness of BPs investigated in this work.

As for the area distributions, those of both iBPs and niBPs for the entire FOV, as well as in Regions A and B, follow log-normal distributions, as displayed in Figure 6. The iBPs in Regions A and B have very similar log-normal distribution patterns (see the middle panel of Figure 6), which are the same for the niBPs, as displayed in the right panel of Figure 6. This result reveals that the area distribution of evolving BPs is independent of the background magnetic fields, which is in agreement with simulations performed by Crockett et al. (2010). We also calculated the equivalent diameter distributions of both iBPs and niBPs. We found that both distributions are log-normal, with average sizes of $163 \pm 27 \text{ km}$ for iBPs and $191 \pm 40 \text{ km}$ for niBPs, respectively. The size distribution of iBPs obtained in our work is in agreement with, e.g., Yang et al. (2014), Feng et al. (2013), Utz et al. (2009), and Abramenko et al. (2010).

Figure 6 also shows that niBPs span a larger range of areas than iBPs. Crockett et al. (2010) found that the BP area distribution follows log-normal statistics, which was thought to be caused by the underlying fragmentation process (Bogdan et al. 1988). They concluded that BPs cannot be observed co-spatial to magnetic flux tubes of large diameters because the energy from the exterior environment as a result of the radiative diffusion may not be enough to heat the relatively tenuous flux tubes of a few 10^2 km in diameter or width (see also discussions of Berger et al. 1995). Beck et al. (2007) also noticed that very few BPs have diameters larger than $0''.4$. Anđić et al. (2011) found only 6% of BPs were larger than $0''.5$. We also observed that some BPs possess laminal or elongated shapes with large areas but small width. In our work, we only obtained five snapshot BPs with diameters larger than $0''.5$ (about 360 km).

As for the intensity contrast of BPs, we found in this work that the values of C_0 defined by Equation (8) followed the Gaussian distribution for both iBPs and niBPs in the entire FOV, and in Regions A and B. To compare our results with those of the other authors who usually discussed the relative brightness, C_0+1 , instead of C_0 , we also evaluated values of C_0+1 , according to Figure 9, and noticed that the values of C_0+1 obtained here varied from 0.8 to 1.3, which is consistent with Ji et al. (2016). Sánchez Almeida et al. (2004) and Langhans et al. (2002) reported these values ranging from 0.8 to 1.8, and Yang et al. (2014) found maximum values between 1.01 and 1.03.

Table 3 shows that the intensity contrast of the iBPs in the entire FOV is somewhat lower than that of the niBPs. This is true for BPs in Regions A and B as well. For both iBPs and niBPs in Regions A and B, intensity contrast distributions share the same mean and width values of the Gaussian distribution. Therefore, we conclude that the intensity contrast distributions of both iBPs and niBPs are independent of background magnetic fields.

Looking into the motion pattern of evolving BPs reveals that about 502 evolving BPs manifested one of two types of rotation: either a change in the orientation of the elongated evolving BP or apparent motions in vortices. For the first type of rotation, we noticed that a typical elongated evolving BP evolves initially into a round one (see Figures 10(a) through (e)), and then becomes elongated into a laminal evolving BP in another direction as the inter-granule lane became narrower (see Figure 10(f)–(j)). In this case, it is not the laminal evolving BP itself that rotates, but rather its shape changes, which gives the apparent impression of a change in its orientation, due to the convective motion of the surrounding plasma.

In the second case, evolving BPs were observed to move in a more complex fashion than in the first case: the evolving BPs displayed splitting and merging as they moved within vortices. The vortex motion is thought to result from spinning of the draining matter because of the conservation of the angular momentum (see also Bonet et al. 2008). Regarding the interaction between evolving BPs and granules nearby, Anđić et al. (2011) and Morinaga et al. (2008) report that the evolution of BPs could confine the development of granules. We noticed, while carrying out this work, that a granule could even vanish or disappear as evolving BPs moved toward it. Contrary to the first scenario in which the convective motion causes changes in evolving BP shapes and orientations, the existence of a high concentration of magnetic flux in an evolving BP could in turn affect, or even suppress, the nearby convective motion as well (see also, e.g., Anđić et al. 2011 and Morinaga et al. 2008 for more details).

These two cases represent different types of motions for evolving BPs. They show us that some BPs evolve passively because of granule convection, whereas other BPs evolve dynamically and can break granules or change the shape of nearby granules. The first scenario changed the evolving BP's shape, and may also have changed the plasma distribution inside the evolving BP as a result of the compression of granules. We need to note here that we ascribed the evolving BP motion in the second case to the existence of a vortex around it, such that the sub-photosphere rotation causes the rotation of evolving BPs observed on the photosphere. Furthermore, twisted flux tubes might release their energy by untwisting, leading to the rotation of evolving BPs as well.

The first type of merging happened when two evolving BPs chased one another along the inter-granule lane, and the following one caught up with the leading one, eventually merging into a large snapshot BP (see Figure 11). In this process, the granule and the inter-granule lane nearby did not show apparent motion or change, so the merging is not likely to result from the convection near the surface, but might be due to the random motion of flux tubes. In the second case, two or more evolving BPs stayed very close before gradually approaching one another and eventually merging. Following this, the granule and the inter-granule lane showed significant change (see Figure 10). Again, the impact of the convection of the surrounding plasma on merging is not obvious, and random motions might result in such merging. Naturally, we also observed the merging due to the convection motion because the inter-granule lane where the evolving BPs were located became narrower than before and the granule aside the merging BPs became brighter at the same time.

One may state that splitting of the evolving BP looked simple and more straightforward. We realized that two causes

could be responsible for the splitting. One is the motion of the granule close to the evolving BP (Figure 14(b)–(d)) that tore a part of evolving BP away from the main part (comparing panels (g) through (j) of Figure 14). Another reason may be an instability occurring inside the laminal evolving BP itself, which tore the laminal evolving BP into several smaller ones. Furthermore, Steiner (1999) also suggested that the interchange instability of the footpoints of the flux tube could be responsible for the fragmentation of evolving BPs. Regarding the interchange instability, interested readers should refer to Priest (2014, pp. 263–264).

5. Conclusion

In this work, we investigated the observational signatures and evolutionary behavior of BPs observed by the NVST. A new algorithm was developed to identify and track both iBPs and niBPs; the former is the evolving BP, which shows simple behavior and is subject to neither splitting nor merging, whereas the latter show complex behavior, including splitting and merging. The FOV of the entire data set is about $69'' \times 62''$, while the studied FOV after removing the sunspot region is 2151.9 Mm^2 , and the three regions (A, B, and C) selected in this work have identical FOV of $19''.5 \times 19''.5$. Among these three regions, Region A contains more evolving BPs and includes two pores with strong background magnetic field. Region B has fewer evolving BPs, but includes several large clusters. Region C behaves most quietly, with the fewest evolving BPs and the weakest background magnetic field among the three regions.

The main results of this work are summarized as follows.

1. We identified 2010 evolving BPs in total, with 64.9% being iBPs and the remaining being niBPs. We found that the number density/area coverage spreads non-uniformly around the sunspots, such that more BPs appeared in Region A, fewer were seen in Region B, and almost no BPs appeared in Region C. The number density of BPs is 0.25 BPs Mm^{-2} on average: it varies from 0.46 Mm^{-2} in Region A, to 0.38 Mm^{-2} in Region B, and 0.02 Mm^{-2} in Region C. The area coverage of BPs is 0.57% for the entire FOV, 1.1% for Region A, 0.82% for Region B, and 0.04% for Region C. This reveals that both the number density and the area coverage of BPs are higher in the regions with stronger background magnetic fields, and lower in the regions with weaker background magnetic fields.
2. Lifetimes of both iBPs and niBPs follow log-normal distributions, and the average lifetimes are $267 \pm 140 \text{ s}$ and $421 \pm 255 \text{ s}$, respectively. About 10% of iBPs (niBPs) have lifetimes longer than 459 s (769 s). For both iBPs and niBPs, the average lifetimes in Region A with strong background magnetic fields are shorter than those in Region B with weaker background magnetic fields.
3. Sizes of both iBPs and niBPs follow log-normal distributions, which do not seem to vary significantly with the background magnetic fields. The area of iBPs is about $(2.15 \pm 0.74) \times 10^4 \text{ km}^2$ on average, and that of the niBP is about $(3.00 \pm 1.31) \times 10^4 \text{ km}^2$, with 10% of snapshot BPs having areas larger than $7.67 \times 10^4 \text{ km}^2$ and $12.3 \times 10^4 \text{ km}^2$, respectively. The size ratio of the iBPs at their vanishing time to that at their first

appearance time ranges from 0.5 to 1.9, and the size ratio at the time with maximum size to that at the first appearance time ranges from 1 to 2.3.

4. The intensity contrast of evolving BPs follows a Gaussian distribution, with the corresponding intensity varying from 0.8 to 1.3 times the average background intensity. The intensity contrast distributions of evolving BPs are independent of the background magnetic fields.
5. Evolving BPs may become elongated when the inter-granule lanes become narrower, and become more circular when the inter-granule lanes widen. During this process, the intensity of evolving BPs is enhanced when they are pushed into a laminal shape in the narrower inter-granule lanes. The evolving BPs change their shape passively under the influence of convective motion. On the other hand, in the case of vortex motions being present, we noticed that several evolving BPs walked clockwise around a granule and eventually even broke the granule.
6. Merging and splitting of evolving BPs have also been studied in this work. We found that merging may take place either when evolving BPs chase each other, when faster ones catch up with the slower ones, when evolving BPs move toward one another with the inter-granule lane around remaining unchanged, or when the surrounding granules expand and push them together. Compared to the merging behavior, the splitting behavior of evolving BPs was simple and straightforward, and might be caused by the convective motion or the instability of the laminal structure itself.

We would like to thank the editor and the referee very much for the very valuable and useful comments that helped improve this paper. This work was supported by Program 973 grant 2013CBA01503, NSFC grants U1631130, 11333007, 11763004, and 11633008, and CAS grants QYZDJ-SSW-SLH012 and XDA15010900, as well as the grant associated with the project of the Group for Innovation of Yunnan Province. The authors thank the NVST group for helping organize observations and for reconstructing high-resolution images. R.E. is grateful to STFC (UK) for the awarded Consolidated Grant, and The Royal Society for giving their support through a number of mobility grants. He also thanks the Chinese Academy of Sciences President's International Fellowship Initiative, Grant No. 2016VMA045 for support received.

ORCID iDs

Yanxiao Liu  <https://orcid.org/0000-0002-3921-1679>
 Yongyuan Xiang  <https://orcid.org/0000-0002-5261-6523>
 Robertus Erdélyi  <https://orcid.org/0000-0003-3439-4127>
 Dong Li  <https://orcid.org/0000-0002-4538-9350>
 Zongjun Ning  <https://orcid.org/0000-0002-9893-4711>
 Yi Bi  <https://orcid.org/0000-0002-5302-3404>
 Jun Lin  <https://orcid.org/0000-0002-3326-5860>

References

Abramenko, V., Yurchyshyn, V., Goode, P., et al. 2010, *ApJL*, **725**, 101
 Abramenko, V. I., Carbone, V., Yurchyshyn, V., et al. 2011, *ApJ*, **743**, 133
 Andić, A., Chae, J., Goode, P. R., et al. 2011, *ApJ*, **731**, 29
 Balmaceda, L., Vargas Domínguez, S., Palacios, J., et al. 2010, *A&A*, **513**, 6

Beck, C., Bellot Rubio, L. R., Schlichenmaier, R., et al. 2007, *A&A*, **472**, 607
 Berger, T. E., Löfdahl, M. G., Shine, R. A., et al. 1998, *ApJ*, **506**, 439
 Berger, T. E., Schrijver, C. J., Shine, R. A., et al. 1995, *ApJ*, **454**, 531
 Bogdan, T. J., Gilman, P. A., Lerche, I., et al. 1988, *ApJ*, **327**, 451
 Bonet, J. A., Márquez, I., Sánchez Almeida, J., Cabello, I., et al. 2008, *ApJL*, **687**, L131
 Bovelet, B., & Wiehr, E. 2001, *SoPh*, **201**, 13
 Bovelet, B., & Wiehr, E. 2003, *A&A*, **412**, 249
 Bovelet, B., & Wiehr, E. 2007, *SoPh*, **243**, 121
 Cao, W., Gorceix, N., Coulter, R., et al. 2010, *AN*, **6**, 636
 Criscuolo, S., & Uitenbroek, H. 2014, *A&A*, **562**, L1
 Crockett, P. J., Jess, D. B., Mathioudakis, M., et al. 2009, *MNRAS*, **397**, 1852
 Crockett, P. J., Mathioudakis, M., Jess, D. B., et al. 2010, *ApJL*, **722**, L188
 De Pontieu, B. 2002, *ApJ*, **569**, 474
 Dunn, R. B., & Zirker, J. B. 1973, *SoPh*, **33**, 281
 Fedun, V., Shelyag, S., & Erdélyi, R. 2011, *ApJ*, **727**, 17
 Feng, S., Deng, L., Shu, G., et al. 2012, in 2012 IEEE Fifth Int. Conf. on Advanced Computational Intelligence, A Subpixel Registration Algorithm FOR Low PSNR Images (New York: IEEE Press), 626
 Feng, S., Deng, L., Yang, Y., et al. 2013, *Ap&SS*, **348**, 17
 Feng, S., Ji, K.-F., Deng, H., et al. 2012, *JKAS*, **45**, 167
 Feng, T., Dai, W., Wang, R., et al. 2017, *AR&T*, **182**, 1672
 Fischer, C. E., Bello González, N., & Rezaei, R. 2016, in ASP Conf. Ser. 504, Coimbra Solar Physics Meeting: Ground-based Solar Observations in the Space Instrumentation Era, ed. I. Dorotovic, C. E. Fischer, & M. Temmer (San Francisco, CA: ASP), 19
 Fried, D. L. 1966, *JOSA*, **56**, 1372
 Gonzalez, R. C., & Woods, R. E. 2008, *Digital Image Processing* (New Jersey: Pearson Education, Inc.)
 Grevesse, N., & Sauval, A. J. 1973, *A&A*, **27**, 29
 Grossmann-Doerth, U., Schüssler, M., & Steiner, O. 1998, *A&A*, **337**, 928
 Harvey, K. L., & Martin, S. F. 1973, *SoPh*, **32**, 389
 Hewitt, R. L., Shelyag, S., Mathioudakis, M., et al. 2014, *A&A*, **565**, A84
 Ishikawa, R., Tsuneta, S., Kitakoshi, Y., et al. 2007, *A&A*, **472**, 911
 Jafarzadeh, S., Cameron, R. H., Solanki, S. K., et al. 2014, *A&A*, **563**, 101
 Jess, D. B., Mathioudakis, M., Erdélyi, R., et al. 2009, *Sci*, **323**, 1582
 Ji, K.-F., Xiong, J.-P., Xiang, Y.-Y., et al. 2016, *RAA*, **16**, 78
 Keller, C. U., Schüssler, M., Vögler, A., et al. 2004, *ApJL*, **607**, L59
 Keys, P. H., Mathioudakis, M., Jess, D. B., et al. 2011, *ApJ*, **740**, 40
 Langhans, K., Schmidt, W., & Tritschler, A. 2002, *A&A*, **394**, 1069
 Liu, Z., Xu, J., Gu, B.-Z., et al. 2014, *RAA*, **14**, 705
 Mehlretter, J. P. 1974, *SoPh*, **38**, 43
 Morinaga, S., Sakurai, T., Ichimoto, K., et al. 2008, *A&A*, **481**, L29
 Möstl, C., Hanslmeier, A., Sobotka, M., et al. 2006, *SoPh*, **237**, 13
 Müller, R. 1983, *SoPh*, **85**, 113
 Müller, R., & Roundier, T. 1992, *SoPh*, **141**, 27
 Mumford, S. J., & Erdélyi, R. 2015, *MNRAS*, **449**, 1679
 Mumford, S. J., Fedun, V., & Erdélyi, R. 2015, *ApJ*, **799**, 6
 Nagata, S., Tsuneta, S., Suematsu, Y., et al. 2008, *ApJ*, **677L**, 145
 Nisenson, P., van Ballegooijen, A. A., de Wijn, A. G., et al. 2006, *ApJ*, **587**, 458
 Pietarila, A., Hinzberger, J., Zakharov, V., et al. 2009, *A&A*, **502**, 647
 Priest, E. R. 2014, *Magnetohydrodynamics of the Sun* (New York: Cambridge Univ. Press)
 Roberts, B., & Webb, A. R. 1979, *SoPh*, **64**, 77
 Roddier, F. 1981, *PrOpt*, **19**, 281
 Rutten, R. J., Kiselman, D., Rouppe van der Voort, L., & Plez, B. 2001, in ASP Conf. Ser. 236, Advanced Solar Polarimetry—Theory, Observation, and Instrumentation, ed. M. Sigwarth (San Francisco, CA: ASP), 445
 Sánchez Almeida, J., Bonet, J. A., Vitičić, B., et al. 2010, *ApJ*, **715**, 26
 Sánchez Almeida, J., Márquez, I., Bonet, J. A., et al. 2004, *ApJL*, **609**, L91
 Schou, J., Scherrer, P. H., Bush, R. I., et al. 2011, *SoPh*, **275**, 229
 Schüssler, M., Shelyag, S., Berdyugina, S., et al. 2003, *ApJ*, **597**, 173
 Shelyag, S., Keys, P., Mathioudakis, M., et al. 2011, *A&A*, **526**, 5
 Spruit, H. C. 1979, *SoPh*, **61**, 363
 Spruit, H. C., & Zweibel, E. G. 1979, *SoPh*, **62**, 15
 Steiner, O. 1999, in ASP Conf. Ser. 183, High Resolution Solar Physics: Theory, Observations, and Techniques, ed. T. R. Rimmele, K. S. Balasubramaniam, & R. R. Radick (San Francisco, CA: ASP), 17
 Steiner, O. 2005, *A&A*, **430**, 691
 Steiner, O., Franz, M., Bello González, N., et al. 2010, *ApJ*, **723**, 180
 Steiner, O., Hauschildt, P. H., & Bruls, J. 2001, *A&A*, **372**, 13
 Stenflo, J. O. 1973, *SoPh*, **32**, 41
 Tatarskii, V. I. 1961, *Wave Propagation in a Turbulent Medium* (New York: McGraw-Hill), 285
 Tokovinin, A., & Kornilov, V. 2007, *MNRAS*, **381**, 1179

- Unno, W., & Ando, H. 1979, [GApFD](#), **12**, 107
- Utz, D., Hanslmeier, A., Möstl, C., et al. 2009, [A&A](#), **498**, 289
- Utz, D., Hanslmeier, A., Müller, R., et al. 2010, [A&A](#), **511**, 39
- Utz, D., Jurčák, J., Hanslmeier, A., et al. 2013, [A&A](#), **554**, A65
- van Ballegooyen, A. A., Asgari-Targhi, M., Cranmer, S. R., et al. 2011, [ApJ](#), **736**, 3
- Vigeesh, G., Fedun, V., Hasan, S. S., & Erdélyi, R. 2012, [ApJ](#), **755**, 18
- Vögler, A., Bruls, J. H. M. J., & Schüssler, M. 2004, [A&A](#), **421**, 741
- Weigelt, G., & Wirtitzer, B. 1983, [OptL](#), **8**, 389
- Weigelt, G. P. 1977, [OptCo](#), **21**, 55
- Wiehr, E., & Bovelet, B. 2009, [CEAB](#), **33**, 19
- Xiang, Y.-Y., Liu, Z., & Jin, Z.-Y. 2016, [NewA](#), **49**, 8
- Yang, Y.-F., Ji, K., Feng, S., et al. 2015, [ApJ](#), **810**, 88
- Yang, Y.-F., Li, Q., Ji, K., et al. 2016, [SoPh](#), **291**, 1089
- Yang, Y.-F., Lin, J.-B., Feng, S., et al. 2014, [RAA](#), **14**, 741
- Yang, Y. F., Qu, H. X., Ji, K. F., et al. 2015, [RAA](#), **15**, 569